Clim Dyn
DOI 10.1007/s00382-012-1614-7

Simulation of glacial-interglacial cycles by simple relaxation models: consistency with observational results

Antonio García-Olivares · Carmen Herrero

Received: 1 June 2012 / Accepted: 22 November 2012

Abstract The model of Paillard and Parrenin (Earth Planet Sci Lett 227:263–271, 2004) was modified to obtain a closer fit to $\delta^{18}O$ and CO_2 time series for the last 800 kyr. The model performance can be improved if its CO_2 sensitivity to I_{65} insolation is eliminated and if different response times are assumed for ablation/accumulation of ice. Correlations between simulated and experimental time series for CO_2 and ice volume V increase from 0.59 and 0.63 to 0.79 and 0.88, respectively. According to these models, terminations are produced by I_{65} amplification through CO_2-T and T-CO_2 feedbacks, in synergy with an extra CO_2 contribution from the deep ocean. This contribution is strongly dependent on ice-sheet extent and ice volume (or alternatively, CO_2 concentration, which is a good proxy of Antarctic temperature) but is insensitive to Southern Ocean (SO) insolation on 21 February (I_{60}). Change of deep SO state may be the "order parameter" for nonlinear deglacial changes. According to these models, 100 kyr periodicity of glacial cycles arises from the characteristic time of Antarctic ice sheet advance to the continental slope.

Keywords Climatic changes · Paleoclimate · Glacial oscillations · Relaxation models · Oceanic CO_2

Electronic supplementary material The online version of this article (doi:10.1007/s00382-012-1614-7) contains supplementary material, which is available to authorized users.

A. García-Olivares (✉) · C. Herrero
Instituto de Ciencias del Mar (CSIC), Ps. Maritim de la Barceloneta, 37-49, 08003 Barcelona, Spain
e-mail: agolivares@icm.csic.es

C. Herrero
e-mail: herrero@icm.csic.es

1 Introduction

Paleoclimatic data of the past 400 kyr show that Antarctic air temperature and CO_2 increased in parallel and almost synchronously (Pepin et al. 2001; Siegenthaler et al. 2005; Fischer et al. 2010), while the rapid warming over Greenland took place during the last half of their change and coincided with a marked decay in continental ice volume (Pepin et al. 2001). These and other observational results (Sowers and Bender 1995; Bard et al. 1996; Monnin et al. 2001) confirm the role of CO_2 as an important amplifier of the glacial-interglacial warming in the South as well as on the global climate, and suggest that the atmospheric CO_2 concentration increased for several millennia before the melting of the northern hemisphere ice sheets (Paillard 2010).

The last nine glacial terminations involved an increase in atmospheric CO_2 concentration of 80–100 ppmv (Petit et al. 1999; Pepin et al. 2001; Siegenthaler et al. 2005; Lüthi et al. 2008). The cause of the glacial CO_2 decline continues to be controversial. Three types of mechanism have been proposed to explain it: (1) those involving an increase in the export rate of organic carbon to the deep ocean, either via increased nutrient availability at low latitudes or via increased efficiency of nutrient usage at high latitudes (Broecker, 1982; Robinson and Sigman 2008); (2) those involving a reduction in the "ventilation" of water exported to the deep Southern Ocean (SO) (Sarmiento and Toggweiler 1984; Siegenthaler and Wenk 1984; Toggweiler and Sarmiento 1985; Watson and Naveira 2006); and (3) those involving changes in ocean chemistry and carbonate flows to the deep sea (Archer and Maier-Reimer 1994). Additionally, "carbonate compensation" (Broecker 1971; Sigman et al. 1998) would help to amplify the effect of any of the three mechanisms on the

Published online: 18 December 2012

CO_2 variation (Hain et al. 2010). The first type of mechanism can be called "export production" and the second one "deep-water ventilation".

The efficiency of deep-water ventilation in glacial and interglacial times could be modified by three major mechanisms:

(a) Changes in the surface-to-deep mixing rate efficiency (Toggweiler 1999; Gildor and Tziperman 2001) and deep-ocean stratification (François et al. 1997; Paillard and Parrenin 2004; Watson and Naveira 2006), forcing a change in the diapycnal flow of deep CO_2-rich water into surface waters. A stratification-dependent vertical diffusion coefficient appears capable to change also the SO overturning rate with additional consequences on the CO_2 oceanic release (Bouttes et al. 2012).
(b) Switching off/on of the Antarctic upwelling at Drake Passage latitudes in cold/warm conditions (Toggweiler et al. 2006). Any process producing a stronger wind stress curl at Drake Passage latitudes would cause a stronger upwelling of deep CO_2-rich water at the SO divergence.
(c) Extended sea ice in the SO produces a "capping" effect on the CO_2 release to the atmosphere during winter (Keeling and Stephens 2001) and a retardation of the overturning rate in the SO due to sea-ice control on the residual circulation (Watson and Naveira 2006; Fischer et al. 2010).

In all three mechanisms, increased CO_2 release is expected during deglaciation periods and is expected to take place mainly in the SO.

Paillard and Parrenin (2004) proposed a model (hereafter PP04) that incorporates very simple parameterizations attempting to represent dense water formation in the SO. Though the model is simple, the results are encouraging because they correctly reproduce the pace and termination times of all the glacial cycles observed.

In García-Olivares and Herrero (2012) this model was calibrated to obtain a better fit with experimental time series of $\delta^{18}O$ and CO_2 available for the last 800 kyr. Starting from the PP04 model, several relaxation models were developed which incorporate simple parameterizations of the feedbacks between CO_2 and ice volume. It was observed that the performance of PP04 can be improved if its CO_2 sensitivity to insolation is eliminated and if different response times are assumed both for absorption/emission of CO_2 and for ablation/accumulation of ice. Correlations between simulated and experimental time series for CO_2 and ice volume V then increased from 0.59 and 0.63 (in our best calibration of PP04) to 0.77 and 0.88, respectively. The method used to obtain these correlations was similar to the one used in the present study and will be explained in Sect. 2. However, the use of a better global optimization with a genetic algorithm in the present study allowed us to increase these two correlations to 0.79 and 0.89 without increasing the number of parameters. Abrupt CO_2 releases lasting 10–20 kyr were found to occur at the beginning of the last nine deglaciations according to this model.

The good fits obtained with the PP04-derived models suggest that the mechanisms that these models incorporate may be important factors controlling glacial-interglacial oscillations. The objective of this work is: (i) to calibrate a set of PP04-derived models to the $\delta^{18}O$ and CO_2 observational time series in order to quantify the maximum observational variance that these simple models are able to explain; (ii) to identify the mechanisms and dynamics that have been incorporated in the PP04-derived models and that are able to produce their good fits; (iii) to explore the most plausible physical interpretations of the mathematical expressions incorporated in these models, which can be interpreted in alternative ways; and (iv) to study the extent to which the mechanisms and dynamics identified in (ii) and (iii) are consistent with state-of-the-art observational results on the dynamics that supposedly cause glacial-interglacial oscillations. The good match obtained with this set of models and the analysis of (i) and (ii) reinforces the hypothesis that some specific mechanisms are the main drivers of glacial-interglacial oscillations, as we will see, and thus suggests which specific mechanisms should be more seriously investigated. At the beginning of the Discussion and Conclusions section, some uncertainties arising from the intrinsic limitations of relaxation models and from the limitations of $\delta^{18}O$ stacks are discussed. Owing to these limitations, these mechanisms can only be ultimately validated by observational confirmation in the real world.

2 The EP, 4τ and 3τ models

The structure of the first PP04-derived models that we will study (EP, 3τ and 4τ) is the following:

$$dV/dt = (Vr - V)/\tau_V \tag{1a}$$

$$dA/dt = (V - A)/\tau_A \tag{1b}$$

$$dC/dt = (Cr - C)/\tau_C \tag{1c}$$

$$V_r = -xC - yI_{65} + z \tag{2}$$

$$C_r = -\beta V + \gamma P(F) + \delta \tag{3}$$

$$F = aV - bA - cI_{60} + d \tag{4}$$

where V and A are dimensionless indexes for global ice volume and extent of the Antarctic ice sheet respectively, C is a dimensionless index for atmospheric CO_2, I_{65} is the

mean daily insolation at 65°N on 21 June and F is the "salty bottom water formation efficiency" variable. F increases when global climate cools (through V) and decreases when continental shelf areas are reduced (through increased A) and when I_{60} (insolation at 60°S on 21 February) increases. P is the deep-ocean CO_2 contribution that depends non-linearly on the parameter F in such a way that P is very small except when F takes negative values. Thus, its behavior is similar to an on/off switch.

The principal variables V, A and C tend exponentially to a reference state V_r, V and C_r at characteristic times τ_V, τ_A and τ_C, respectively. V_r decreases when C increases, and when I_{65} is high. C_r increases when the oceanic pulse of CO_2 is *on*, and decreases when the ice volume increases. The β parameter represents the positive feedback between temperature and CO_2 (through the ice volume V). The parameter δ can be interpreted as a CO_2 reference-level that is constant or dependent only on long-term geological changes.

Daily insolation for the last 800 kyr is obtained from the Berger (1978) and Berger and Loutre (1991) software. Insolation is normalized with its standard deviation to obtain I_{65} and I_{60}. No lower bound is imposed on the V, C and A variables.

The PP04 model includes direct forcing of the $I_{65}(t)$ insolation on the CO_2 response. The physical interpretation of this forcing is not clear because the CO_2 response to ice volume is already included in the model. Because the best fits of the PP04 model were obtained when this forcing is zero or extremely small (García-Olivares and Herrero 2012), we have eliminated it in the modified models we study in this section. This is the only difference between our Eqs. (1a), (1b), (1c)–(4) and those used by Paillard and Parrenin (2004). Another difference between the models is that, in ours, two different response times are used for accumulation and ablation of ice: $\tau = \tau_{V1}$ for periods when $V < V_r$ and $\tau = \tau_{V2}$ when $V > V_r$.

In one version of these modified models, hereafter called 4τ, the oceanic contribution $P(F)$ was maintained equal to $H(-F)$, where H is the Heaviside function ($H = 1$ if $F < 0$; $H = 0$ otherwise), as in the original model, which generates oceanic CO_2 pulses with a strong non-linear dependence on the stratification parameter F, in the form of a rectangular pulse. Thus, during most glacial periods the oceanic contribution is zero. An alternative way to generate saw-tooth-like oscillations in the glacial periods could be to allow for some non-zero CO_2 emission when F is positive but small. Thus, in the other version, hereafter called "Exponential Pulse" (EP), the previous model was modified by defining P as a function exponentially dependent on F:

$$P(F) = e^{-\lambda F} \quad \text{if} \quad F > 0 \quad \text{and} \quad P(F) = 1 \text{ elsewhere.} \tag{5}$$

The 4τ and EP models also use two different response times for accumulation and absorption of CO_2: $\tau = \tau_{C1}$ for the periods when $C < C_r$ and $\tau = \tau_{C2}$ for periods when $C > C_r$.

The genetic algorithm included in the Matlab software[1] was used to obtain the best fits of both models with the two experimental time series. Figures 1 and 2 of Online Materials show the best fits of the two models. The first panel of Fig. 1 (2) of Online Materials shows the ice volume V (CO_2) predicted by the EP model, while panel 3 shows the ice volume V (CO_2) predicted by the 4τ model. The simulations are compared with the experimental time series: the $\delta^{18}O$ time series (Lisiecki and Raymo 2005), which is a proxy for the global ice volume, and the experimental time series available for CO_2 (Indermühle et al. 2000; Monnin et al. 2001; Petit et al. 1999; Siegenthaler et al. 2005; Lüthi et al. 2008). In all the panels, the time series were normalized by their standard deviation before plotting. The correlations between the predicted and the corresponding observational time series are 0.85 and 0.89 for ice volume and 0.77 and 0.79 for CO_2.

Table 1 of Online Materials show the parameter values corresponding to these two models. For both cases, best fits were obtained for values of parameter c that were so small that almost identical correlations could be obtained for a second parameter set with $c = 0$ (no sensitivity to I_{60} forcing). These final parameter sets are shown in the corresponding column of Table 1, in Online Materials.

The C series in both models shows a saw-tooth form, which is produced by the feedback V–C (through β) in conjunction with the large value used for the parameter τ_{C2} (7,600 and 17,667 years, respectively). The 21- and 42-kyr oscillations are transmitted to C from the V time series through the parameter β, which takes close values for the two cases (0.48 and 0.41, respectively).

The different scale for uptake and release in our models represents the different sequence of events that take place during glacial and interglacial periods, which cannot be reproduced in detail by PP04-derived models because of their excessive simplicity in the representation of carbon processes (see Discussion and Conclusions section). The 4τ model is, however, not very sensitive to the use of a single τ_C for CO_2 uptake/release, since its best calibration with only 13 parameters gives us correlations of 0.88 and 0.79 for V and C, respectively. The resulting model will be called 3τ hereafter.

As can be observed in the first panel of Fig. 1 (3τ model), many details of the high-frequency oscillations of

[1] Matlab is a trademarks of The MathWorks, Inc.

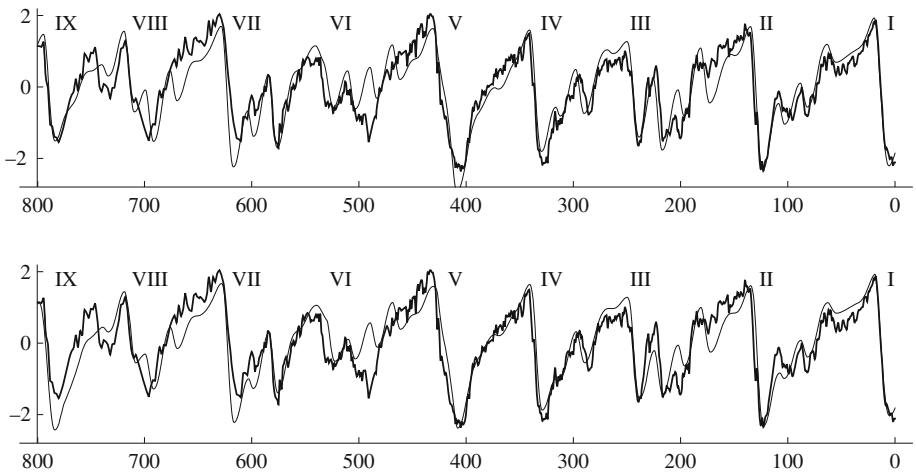

Fig. 1 Ice volume, *V*, predicted by the 3τ and LS models (*thin line* of panels 1 and 2, respectively) compared with $\delta^{18}O$ experimental time series obtained by Lisiecki and Raymo (2005) (*thick line*). Units of the *horizontal axes* are kyr

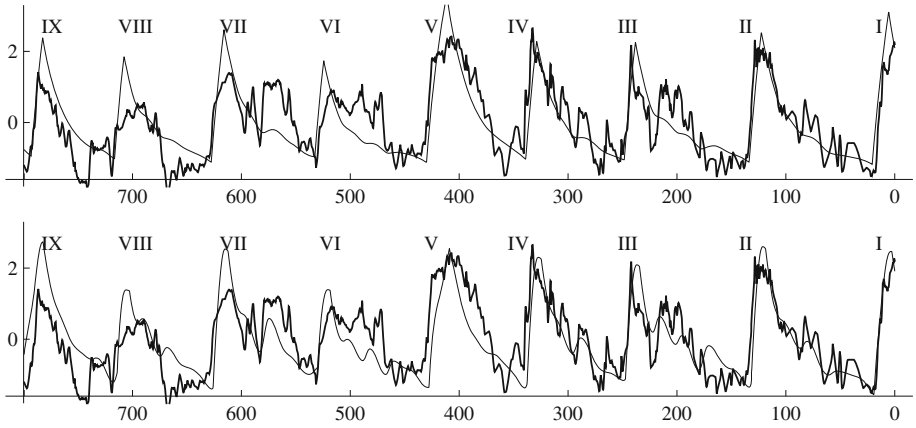

Fig. 2 CO_2 predicted by the 3τ and LS models (*thin line* of *panels 1* and *2*, respectively) compared with experimental time series for CO_2 (*thick line*). Units of the *horizontal axes* are kyr

the experimental ice volume are suitably simulated. The minima at 700 and 575 kyr are similar to the experimental data and the maximum at 220 kyr is closely simulated by this model. The shape of the cycles I, III, IV and VII BP are also closely simulated.

However, 3τ is poor at accurately simulating the minimum of *V* at 200 kyr (cycle II), the *V* minimum at 490 kyr and the maximum ice volume at 750 kyr BP.

In all the models, an almost identical optimum can be found with a set of parameters that does not use the I_{60} forcing (i.e. $c = 0$). This forcing was included in PP04 model to take into account possible regional temperature variations which could affect the freezing of surface waters on the Antarctic shelf. Similarly, *F* dependence on *V* was introduced to take into account the possible effect of global climate cooling and warming (through *V*) on regional climate (Paillard and Parrenin 2004, p. 266). It led us to look for a variable that could represent better than *V* and I_{60} the regional temperature. This variable was the CO_2, as represented in the model by the variable C, and the new model was called "Local Stratification" (LS) model.

3 The LS model

Atmospheric CO_2 can be considered a proxy of Antarctic temperature as shown by the Antarctic deuterium record (Petit et al. 1999; Jouzel et al. 2007; Lüthi et al. 2008), so modeled variable *C* can be considered an approximate proxy of local temperature in the SO. Consequently, a new sub-model has been developed in which I_{60} insolation has been replaced by variable *C*. In the new model, the expression for F was:

$F = aV - bA - cC + d$. However, the best fits obtained for this model did not improved that obtained with $a = 0$. For this reason, we used the final expression (9) that uses one less parameter. Stratification is thus considered dependent only on regional variables (the extent of Antarctic ice sheet *A* and SO temperature, related to $-C$). In parallel with it, it was assumed that SO temperature, as represented by variable *C,* led also the evolution of ice sheet *A* (Eq. 6b). This change has no effect on the correlation obtained for *V* but it improves slightly the correlation obtained for *C*.

Table 1 Parameters used by the 3τ and LS models (lines 2–17) and correlations obtained for the C and V variables (last two lines)

Parameter	3τ	LS
α	–	0.237
β	0.336	0.793
γ	2.044	1.955
δ	0.228	0.146
x	0.905	0.669
y	0.489	0.527
z	0.946	0.761
a	0.54	–
b	1.205	0.936
c	–	0.533
d	0.483	0.069
τ_c	13,505	2,793
τ_{c2}	–	8,414
τ_v	16,585	11,325
τ_{v2}	3,105.5	2,325
τ_A	9,004	10,266
Corr C	0.79	0.76
Corr V	0.88	0.87

Numeric values correspond to the best fits obtained. The parameter set corresponding to LS is the optimum found for both the interval (−600, −200 kyr) and the complete interval (−800 kyr, 0) and the correlations obtained are approximately the same with two digits of precision

The mathematical expression of LS model is the following:

$$dV/dt = (V_r - V)/\tau_V \tag{6a}$$

$$dA/dt = (-C - A)/\tau_A \tag{6b}$$

$$dC/dt = (C_r - C)/\tau_C \tag{6c}$$

$$V_r = -xC - yI_{65} + z \tag{7}$$

$$C_r = \alpha I_{65} - \beta V + \gamma H(-F) + \delta \tag{8}$$

$$F = -bA - cC + d \tag{9}$$

The model was calibrated in a similar way to that explained for the EP, 3τ and 4τ models. The last column of Table 1 shows the parameter values obtained for the best fit. In contrast with 3τ and 4τ, LS has sensitivity to the α parameter (direct I_{65} influence on C_r).

The best correlations (0.76 and 0.87 for C and V, respectively) are close to those of the EP and 3τ models. The best-fit parameters are displayed in the last column of Table 1. The good fits obtained from the LS model suggest that stratification may be controlled by variables with regional influence (A and C).

Panel 2 of Figs. 1 and 2 shows the ice volume and CO_2 predicted by this model. It reproduces high frequencies in the CO_2 curve better than the 3τ model does, though not always in phase with the observational curve, and it is able to reproduce the timing of almost all ice-volume cycles. However, it has problems reproducing the shape of Termination IX. The glacial cycle between 600 and 700 kyr BP remains relatively difficult to simulate.

4 Mechanisms and dynamics of the PP04-derived models

Because the correlation obtained for C with the EP model does not improve upon that obtained with the 4τ model and the correlation for V is even worse (Table 1 of Online Materials), we can conclude that the results obtained do not justify the introduction of an additional parameter. However, the extra contribution to glacial CO_2 produced in this model makes it possible to fit the experimental CO_2 series with a lower value of the y parameter (sensitivity to I_{65} forcing), which produces a V time series with the high-frequency oscillations more damped. The "texture" of this series, as can be observed in Online Materials (Fig. 2, panel 1), resembles that observed in the experimental data.

The performance of 4τ and 3τ models in the simulation of V is quite similar (Online Materials, Fig. 1, panels 2 and 3), except for Termination V and the glacial cycle II (see also Online Materials, Fig. 3), where 4τ performs slightly better. For these reasons, its correlation for V is slightly better (0.89 instead of 0.88). The use of a different relaxation time for emission and absorption of CO_2 allows 4τ to match CO_2 in glacial cycle 5 better than 3τ (Online Materials, Fig. 2, panels 2 and 3). However, the extreme simplicity of the carbon model is shown in both models in the inexistence of high-frequency oscillations in the evolution of C. The LS model has a larger content of high-frequency variance than 3τ because it permits a direct forcing of I_{65} to C but its C correlation is not better because this variance is frequently out of phase with the observational one.

We have obtained four different fits with ice volume correlations between 0.85 and 0.89 which show a good quantitative and qualitative agreement with the empirical time series, except for the warm event of 490 ky BP, which is not reproduced by any model.

The 4τ model improves the PP04 correlations (0.59 and 0.63) to 0.79 and 0.89 using the same number of parameters (14). The EP model uses 15 parameters but the additional parameter, which was aimed at improving the form of the oceanic pulse function, did not improve the correlations and can be considered useless. The 3τ model obtains almost the same correlations as 4τ using only 13 parameters. The LS model (15 parameters) does not improve the correlations of 4τ (which are slightly higher) but incorporates a functional form for stratification F that

seems more consistent with both the mechanisms suggested by Paillard and Parrenin (2004) and with other contributing mechanisms reported in the literature (see "Discussion and Conclusions"). If our aim were to select the model with the best explained variance per parameter, the choice would be 3τ. However, a second objective of this work is to determine whether models with an explained variance similar to the one obtained by 3τ contain parameterizations that can be related as realistically as possible to observed mechanisms. And LS can offer a valuable insight into the real meaning of the good performance of PP04-derived models (see "Discussion and Conclusions"). Hereafter, the dynamics and mechanisms incorporated in 3τ and LS models will be analyzed and compared.

One limitation of the methodology used in this study that is general in paleoclimate models is that there is no distinction between calibration data and validation data. For this reason, it may be useful to know whether parameter optimizations obtained on half of the data interval lead to nearly the same best estimates. Our models seem to fit better the saw-tooth oscillations that climate has shown in the last 400 kyr than the more irregular oscillations occurring between 800 and 400 kyr BP. In order to include both kinds of dynamics, we used the interval −600 to −200 kyr as calibration data in the LS model. This interval led to a best fit that is coincident with the one shown in the last column of Table 1, and the correlations obtained were 0.872 and 0.763, which are slightly better than those obtained for the complete interval (0.866 and 0.757). We have rounded the latter results to two decimal digits in the last column of Table 1. When a second and more exhaustive searching is implemented around the values obtained by the genetic algorithm, it is possible to find a different parameter combination with even better correlations (0.884 and 0.774). However, the case is then so tightly fitted to the calibration interval that it fails to reproduce the pace of the whole interval (and correlations drop to 0.43 and 0.22).

On the other hand, the experimental data used ($\delta^{18}O$: Lisiecki and Raymo 2005; CO_2: Indermühle et al. 2000; Monnin et al. 2001; Petit et al. 1999; Siegenthaler et al. 2005; Lüthi et al. 2008) contain much high-frequency variance, representing (among other things) weather noise, measurement error, and annual-to-centennial climate variability. PP04-derived models do not contain mechanisms able to produce significant variance in these time scales. For this reason, in one of our runs we smoothed these data with a moving average of 2 kyr, and then calibrated the LS model with these time series and the complete interval (-800 ky, 0 ky). The correlations obtained were 0.869 and 0.761, respectively, whereas the result with unfiltered data was 0.866 and 0.756, respectively. In conclusion, the smoothing of the experimental time series provides an improvement of less than 1 % in the fits of the two variables.

The Lisiecki and Raymo (2005) record is a stack of $\delta^{18}O$ data from benthic foraminifera, and the $^{18}O/^{16}O$ ratio is known to depend on both the isotopic composition and the temperature of the water where foraminifera develop. Waelbroeck et al. (2002) found that the relationship between $\delta^{18}O$ and ice volume is not linear, since $\delta^{18}O$ decreases faster than the increase in ice volume at the beginning of the last glaciations, and then progressively more slowly until the ice sheets reached their maximum size. This may produce uncertainties of 20 % for the ice volume estimations at the beginning of glaciations. Consequently, there is some risk of over-interpretation when model parameters are adjusted to fit that isotopic record tightly. If that error were assumed to take place during 20 kyr at the beginning of each glacial period, it would cause a 7 % loss of explained variance or a 4 % loss of correlation. This is slightly above the correlation differences in the four models that we have studied, so their performance must be considered equivalent within the observational uncertainty. For this reason, in our study all four models have been considered to have a suitable fit to the observational series, and the small improvement in correlation obtained with the 4τ model in comparison with the LS and 3τ models was not considered significant to distinguish the structure of this model as better than the other structures studied.

Bintanja et al. (2005) tried to eliminate the temperature effects from the $\delta^{18}O$ series by using a model for air and deep ocean temperatures. The resulting sea-level time series can be used as an alternative to $\delta^{18}O$ (Online Materials, Fig. 3). When we calculated the correlations between this time series and the V predicted by our models, we obtained the surprising result that they increase from 0.88 to 0.90 for 3τ and from 0.87 to 0.89 for LS. This shows that the calibration of our selected models to an isotopic series with experimental biases has produced a robust result in spite of the observational uncertainty. In Online Materials (Fig. 4) the V predicted by 3τ and LS model, as well as EP and 4τ models, are compared with the relative ice volume inferred from the Bintanja (2005) sea-level time series. In most of his sea level timeseries, Bintanja reports one-sigma error of about ±10 m. These margin errors have been used for the whole series in that figure. As can be observed, the predictions of model 3τ are most of time between the error margins or close to them, except punctual moments such as −660, −620, −485 and −200 kyr. The behavior of LS model is almost as good, reinforcing the robustness of the fits implemented.

Wavelet transform, cross-wavelet transform and wavelet coherence are tools that may also be useful for comparing an observational and a simulated time series,

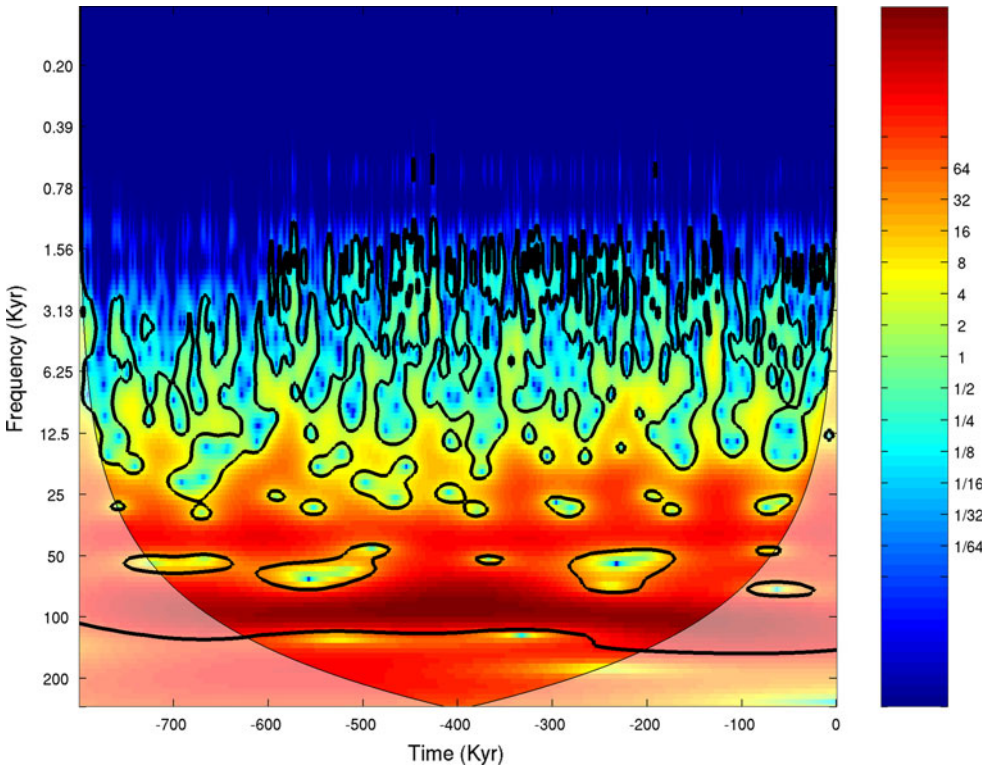

Fig. 3 Wavelet diagram of the $\delta^{18}O$ time series used in our study

complementing the information obtained from correlation coefficients. Figures 3, 4 and 5 show the wavelet transform of the $\delta^{18}O$ and *V* time series of the 3τ and LS models. Units in the color bar are wavelet transform power, i.e. $|W_i|^2$, where W_i is the wavelet transform or convolution between the Morlet wavelet function and the time series and "*i*" designates the position of datum number *i*. The thick black line above and below Figs. 4 and 5 (as well as in all the figures created by this software hereafter) designates the 95 % significance level against red noise and the thin black line designates the cone of influence where edge effects might distort the field. The Matlab Cross-wavelet and wavelet coherence software by Grinsted et al. (2004) (available at: http://www.pol.ac.uk/home/research/waveletcoherence/) was used for calculations.

As shown in Figs. 3, 4 and 5, the 100-kyr band is the dominant period in both the $\delta^{18}O$ and *V* time series of the 3τ and LS models, followed by the 42-kyr band, and power in both frequencies is similarly distributed in observational and simulated series. The $\delta^{18}O$ time series contains periodicities in the range 1–10 kyr; in contrast, our models do not generate any significant periodicity under 10 kyr. The 21-kyr period is weakly present in both experimental and 3τ time series. The LS and 3τ models show the same patterns in their wavelet diagrams, which are almost indistinguishable from each other.

For CO_2 (Figs. 6, 7 and 8) the power distribution in the simulated and observational time series are similar for the 100-kyr band. Power in the 42-kyr band is somewhat more homogeneously distributed in the observational time series than in the simulated time series. The 21-kyr contribution is weaker in both series and is distributed in a different way in the modeled and observational time series. The difference is greater in the first three cycles, which are relatively difficult to model.

Power spectra of observational and simulated time series were also obtained with Fast Fourier Transform and they are shown in Fig. 9 for observational ice volume and *V* simulated by 3τ and LS, respectively, and in Fig. 10 for the observational CO_2 and *C* simulated by the same models. As can be observed, frequency content is similar in observational and simulated time series for both the *V* and *C* variables. However, $\delta^{18}O$ has 10 % more power content in the band of 100 kyr and 15 % more power content in the 41 kyr band than the *V* predicted by our models. Power in 23 kyr band is small in observational and simulated time-series. Regarding the *C* variable simulated by 3τ, the observational and simulated spectra are more similar than those for *V*, in spite of the worse correlations obtained for *C*. However, LS tends to under-predict the 100 kyr power content and to over-predict the power in 41 and 23 kyr bands.

The complex cross-wavelet transform of two time series (Figs. 11 to 14) can be interpreted as the shared power in a given periodicity band (absolute value) and the phase between the two series in time frequency space

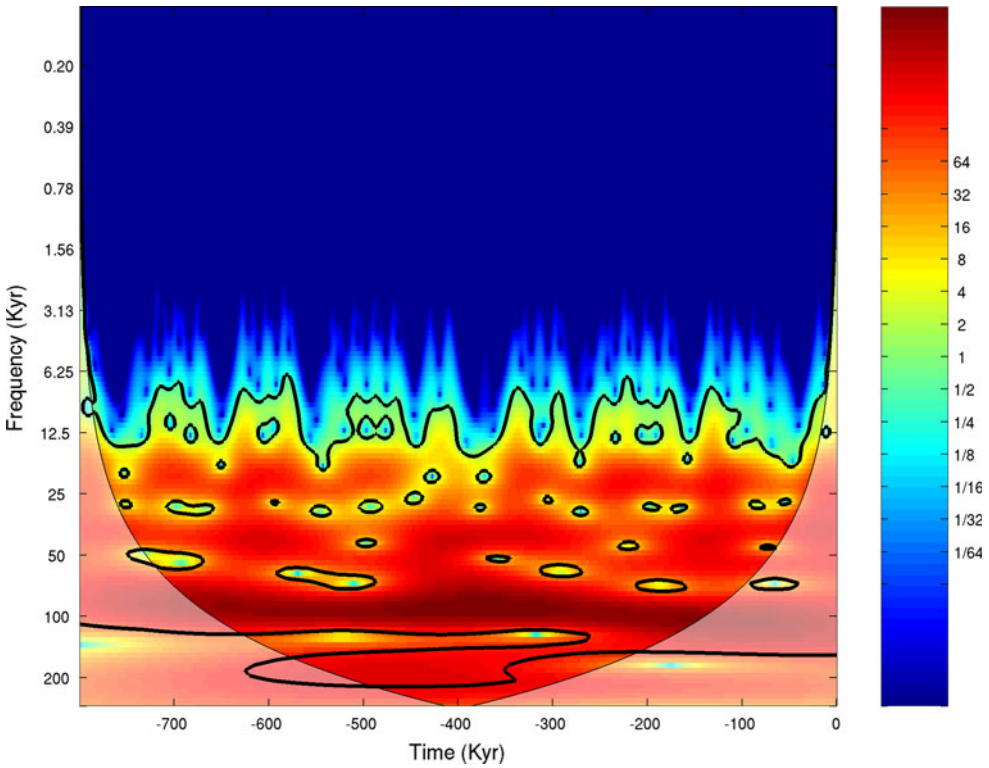

Fig. 4 Wavelet diagram of the V time series calculated by the 3τ model

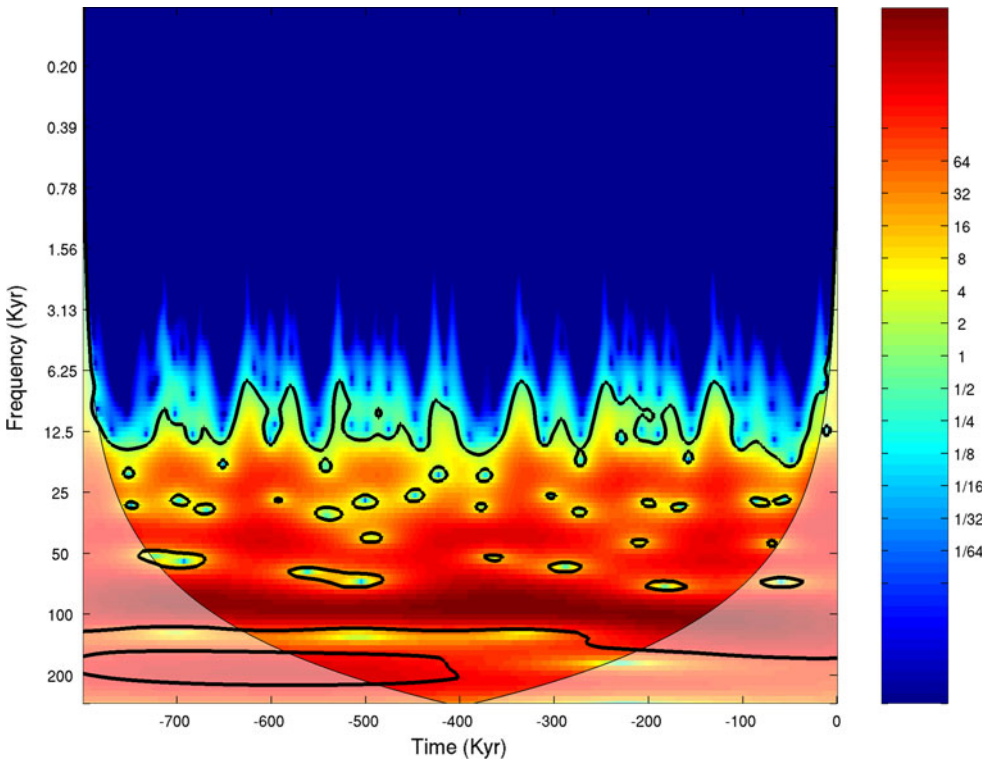

Fig. 5 Wavelet diagram of the V time series calculated by the LS model

(Grinsted et al. 2004). Darker red color indicates greater shared power in that time and periodicity band, and the arrow angle indicates the phase between the observational and simulated series.

As can be observed in Fig. 11 and 12, observational and simulated ice volume share a great common power in the 100 and 42-kyr band. In the 100-kyr band the two periodicities are in phase, but in the 42-kyr band the modeled

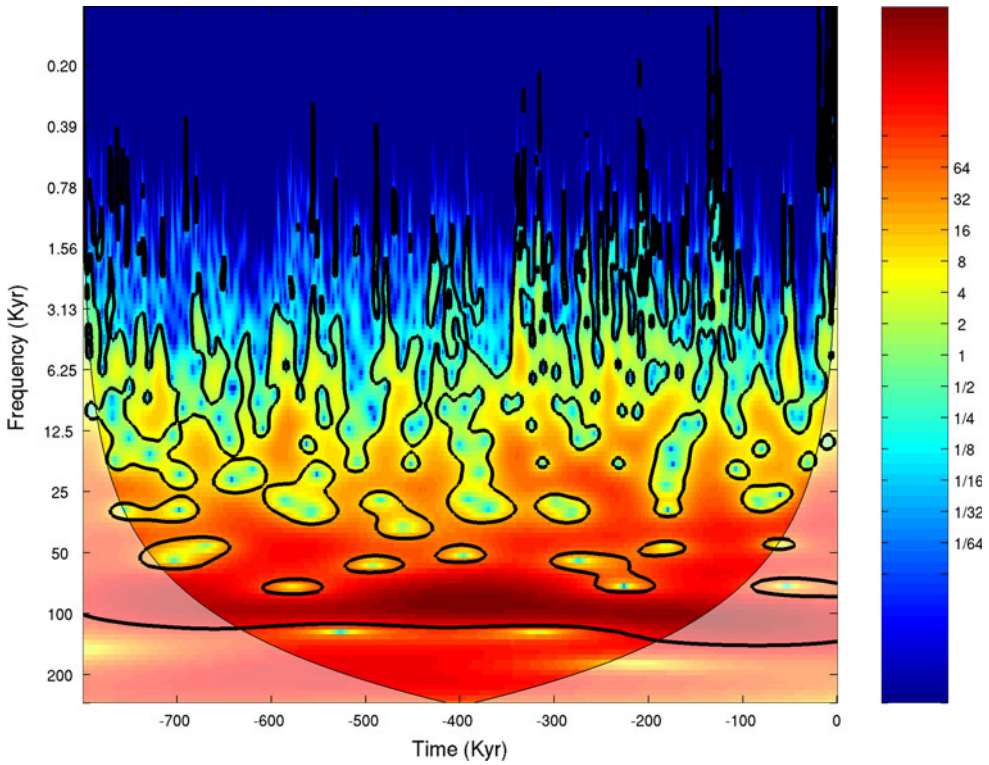

Fig. 6 Wavelet diagram of the CO_2 time series used in our study

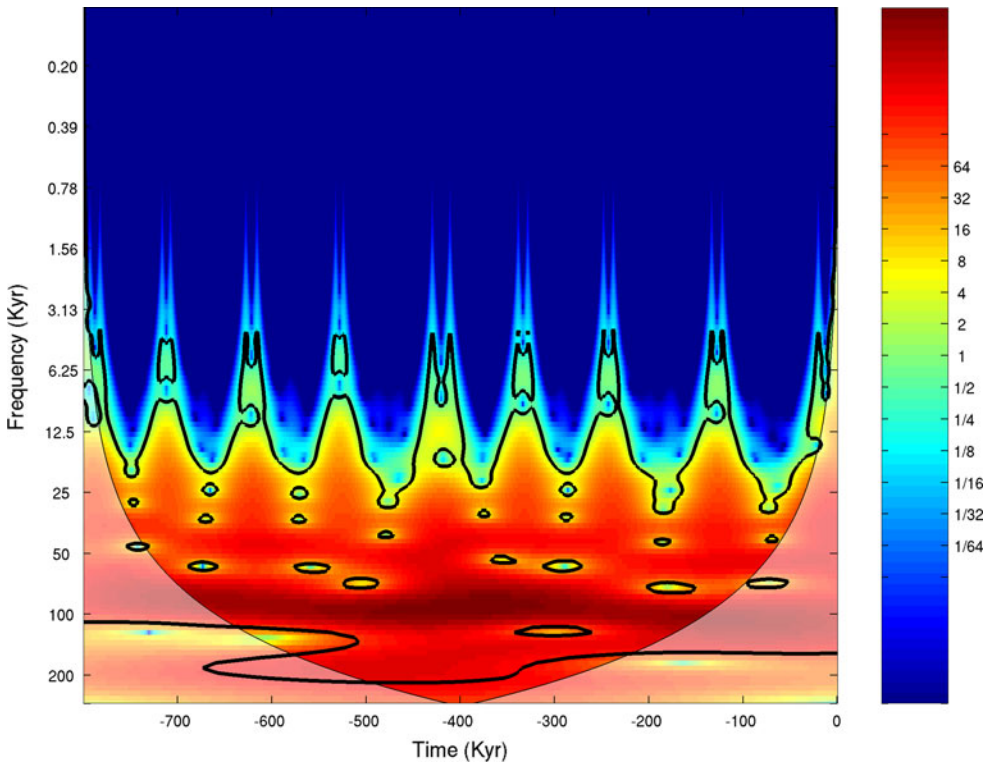

Fig. 7 Wavelet diagram of the *C* time series calculated by the 3τ model

periodicity tends to lead the observational one at some moments, with a phase of between 0 and π/4. In the 41 and 23-kyr band the two periodicities tend to be in phase when the common power is high and out of phase when the shared power is low. The two models studied (3τ and LS) show very close patterns in their cross-wavelet transforms for *V*.

Regarding CO_2 (Figs. 13 and 14), the largest shared power is in the 100-kyr band, especially after −500 kyr,

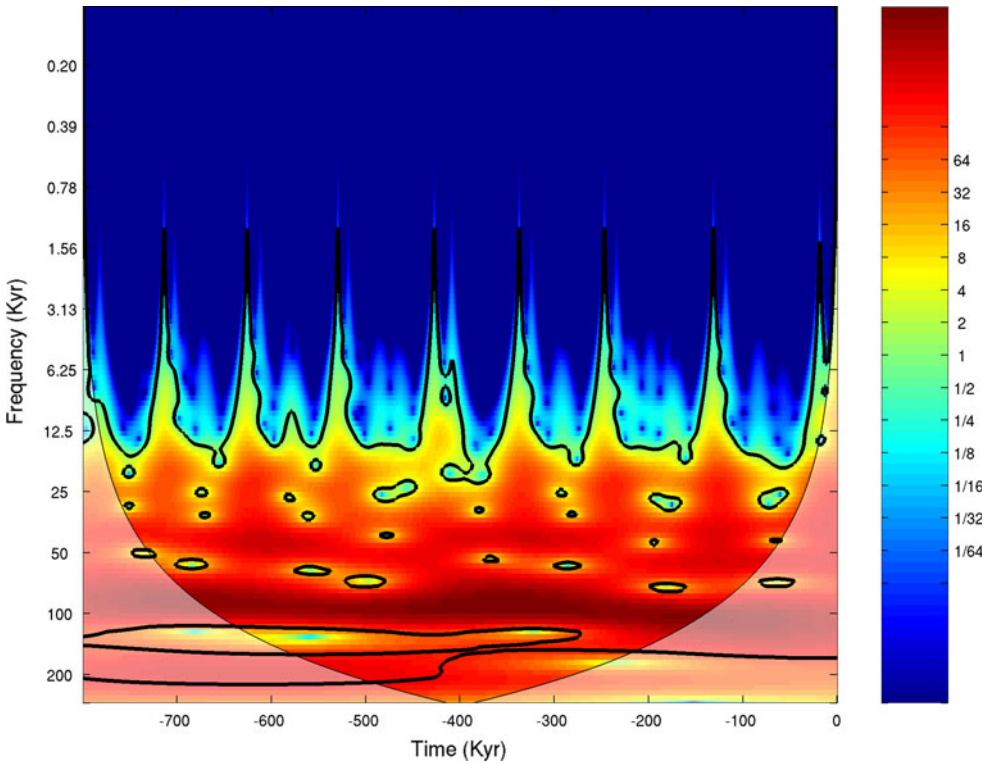

Fig. 8 Wavelet diagram of the *C* time series calculated by the LS model

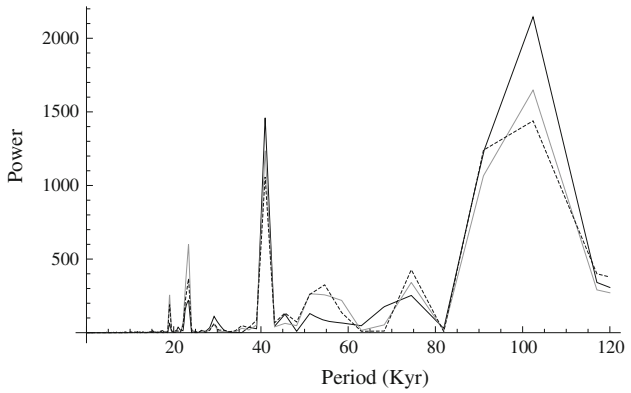

Fig. 9 Power spectrum of $\delta^{18}O$ (*continuous line*) and *V* timeseries calculated by 3τ (*gray line*) and LS models (*dashed line*)

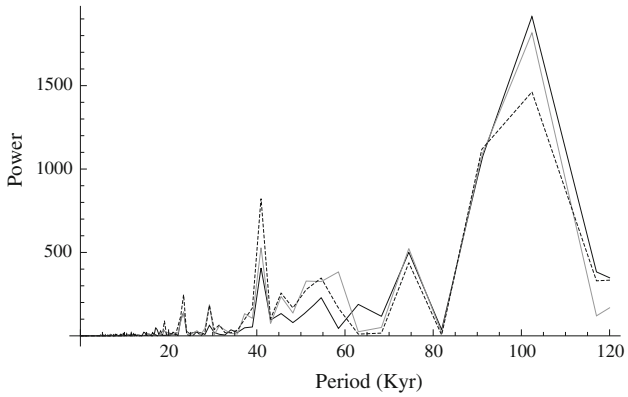

Fig. 10 Power spectrum of CO_2 (*continuous line*) and *C* timeseries calculated by 3τ (*gray line*) and LS models (*dashed line*)

when the fit between simulated and observational cycles is somewhat better (see Fig. 2). In the 42-kyr band the shared power is lower and has relative maxima around −600 kyr, between −400 and −200 kyr and between −150 and −50 kyr. These intervals of good coincidence can be also observed in Fig. 2 for the LS model. Low shared power is observed in the 21-kyr band, with an out-of-phase pattern in some intervals.

Wavelet coherence of two series can be interpreted as a localized correlation coefficient in time frequency space. It is useful to find locally phase-locked behavior, that is, moments in which both series oscillate with the same frequency and a given phase difference. Figures 15 and 16 show the wavelet coherence of the $\delta^{18}O$ and the simulated *V* series for 3τ and LS, respectively, and Figs. 17 and 18 show the wavelet coherence of the observational CO_2 and the simulated *C* series for the same models. It can be observed that the correlations of *V* for the two models are always in phase, are larger than 0.9 in the 100 kyr band for all times and are especially high in the four last cycles (−400 kyr to 0). In the 41-kyr band the simulated and observational series oscillate together with a correlation >0.9 around −600 kyr, between −400 and −350 kyr and between −130 and −90 kyr and always greater than 0.7. The coherence is negligible between −750 and −630 kyr

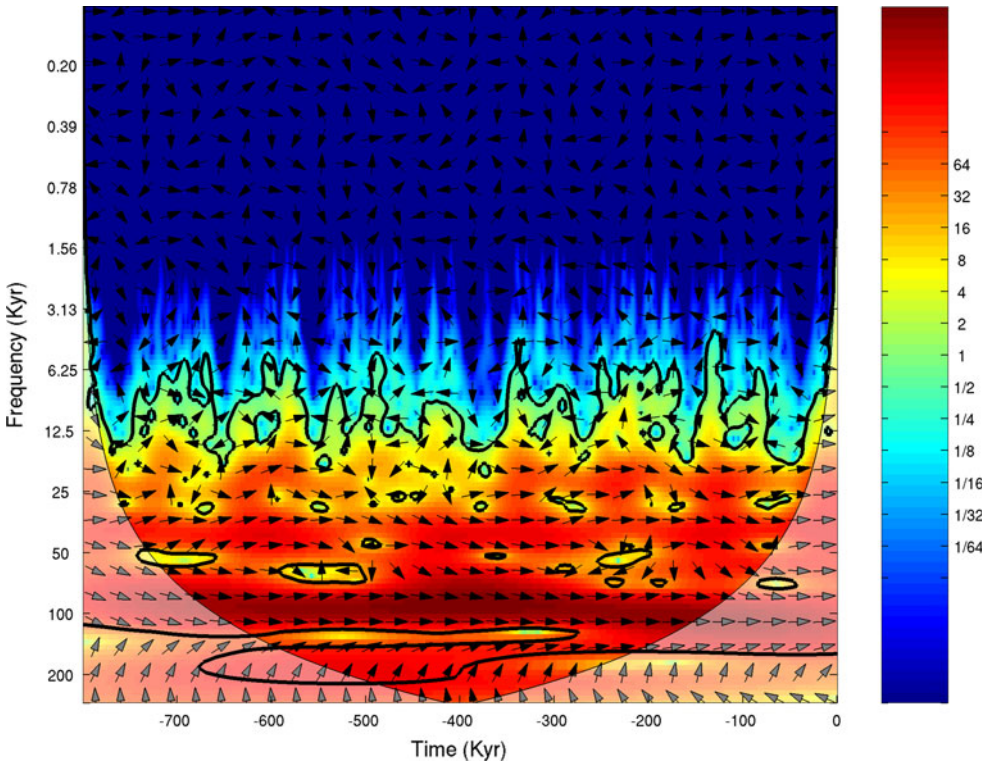

Fig. 11 Cross-wavelet transform of $\delta^{18}O$ and V calculated by the 3τ model

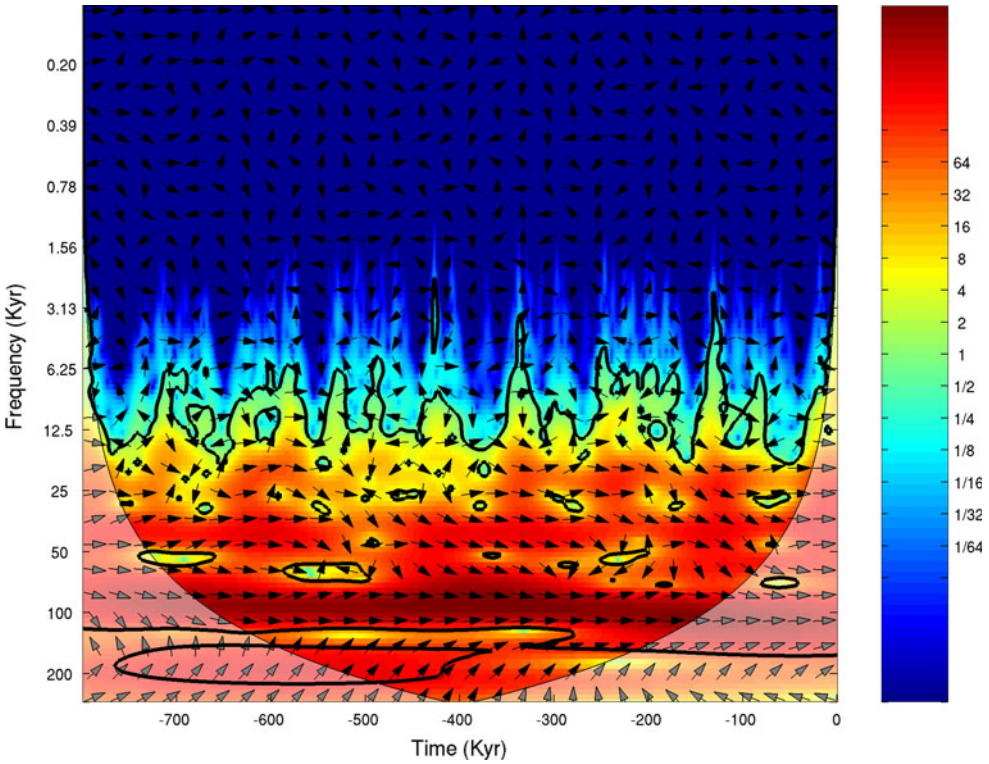

Fig. 12 Cross-wavelet transform of $\delta^{18}O$ and V calculated by the LS model

and between −540 and −380 kyr, corresponding to intervals in which the models are worse at matching the observational series (see also Fig. 1).

Regarding CO_2 (Figs. 17 and 18), in the two models (3τ and LS, respectively) the coherence in the 100-kyr band is in phase and strong after −500 kyr and weaker and out of

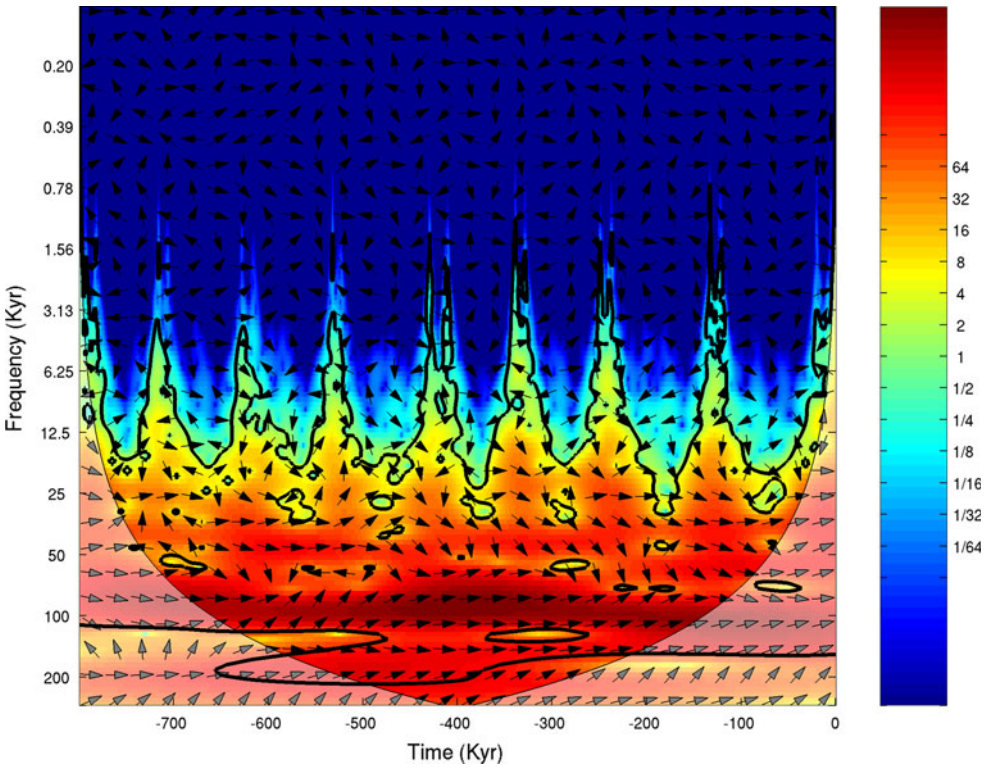

Fig. 13 Cross-wavelet transform of CO_2 and *C* calculated by the 3τ model

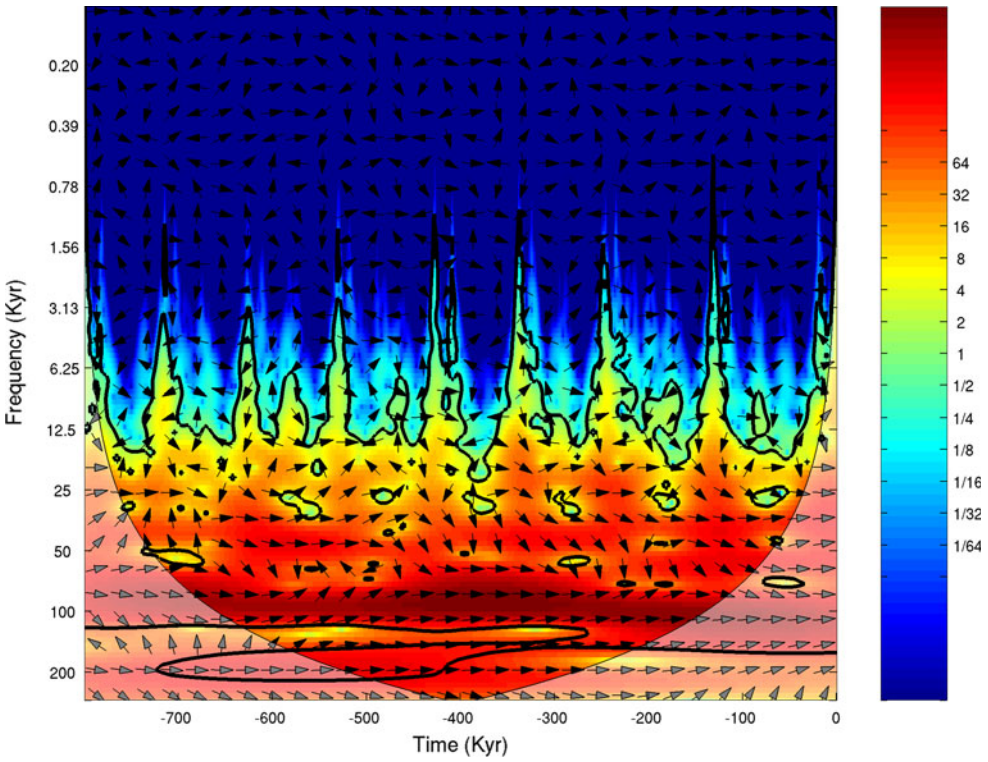

Fig. 14 Cross-wavelet transform of CO_2 and *C* calculated by the LS model

phase before −500 kyr coinciding with the first glacial cycles (see also Fig. 2), which are more difficult to simulate. In the 42-kyr band the coherence is high in roughly the same intervals as in the V series, and in the 21-kyr band it is practically inexistent. This can be attributed to the combined effects of high-frequency damping produced by parameter τ_C (and/or τ_{C2} in LS) and poor representation of the carbon dynamics by PP04-derived models.

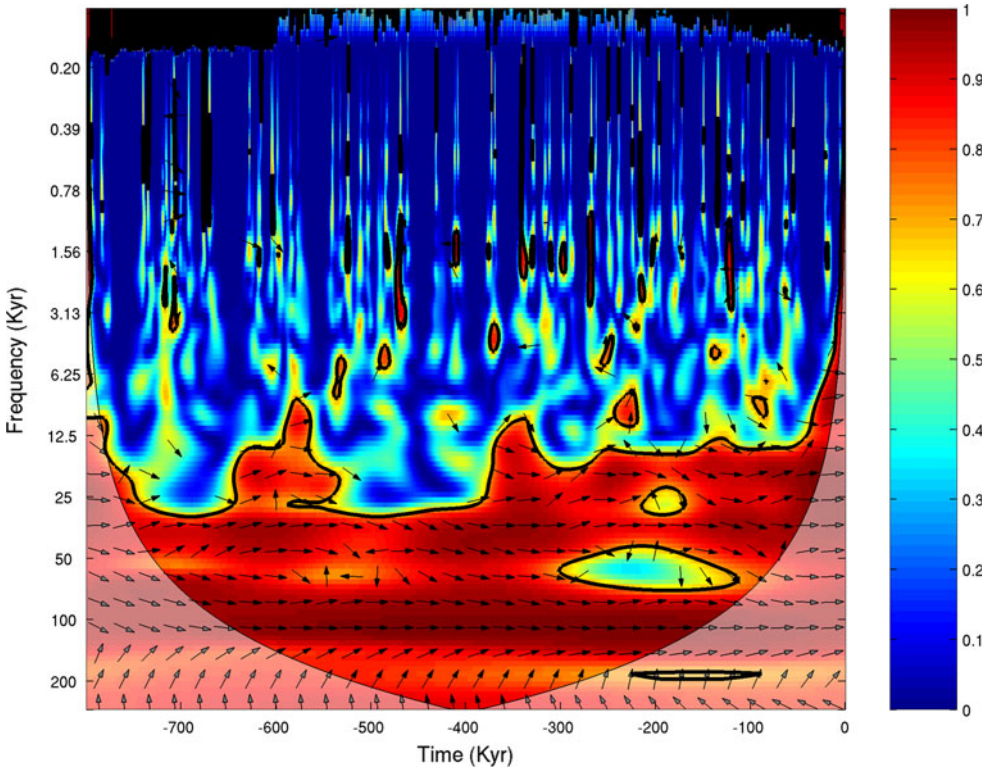

Fig. 15 Wavelet Coherence of $\delta^{18}O$ and *V* calculated by the 3τ model

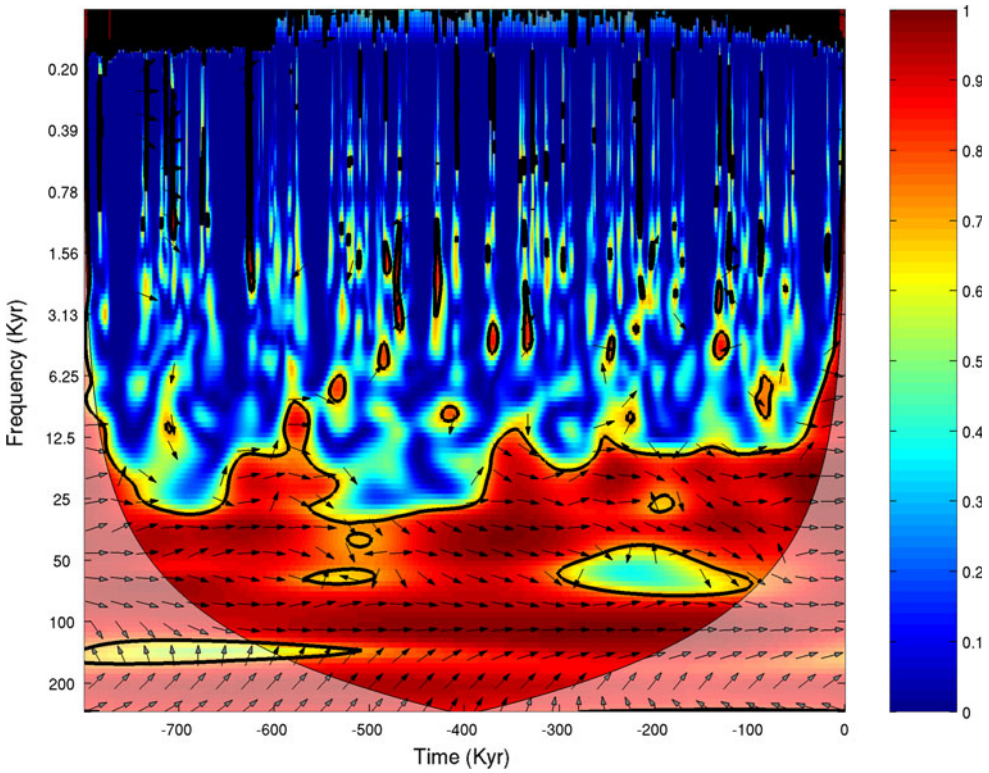

Fig. 16 Wavelet Coherence of $\delta^{18}O$ and *V* calculated by the LS model

Phase space portraits and embedding attractor techniques can also be useful for quantifying the performance of a simulated time series in matching the dynamical properties of an observational time series. Time series of 16001 linearly interpolated, equally spaced data were used to reconstruct the attractors. To avoid autocorrelated effects we used the method of mutual information, which estimated an optimal time lag between data to be used of 1,433.

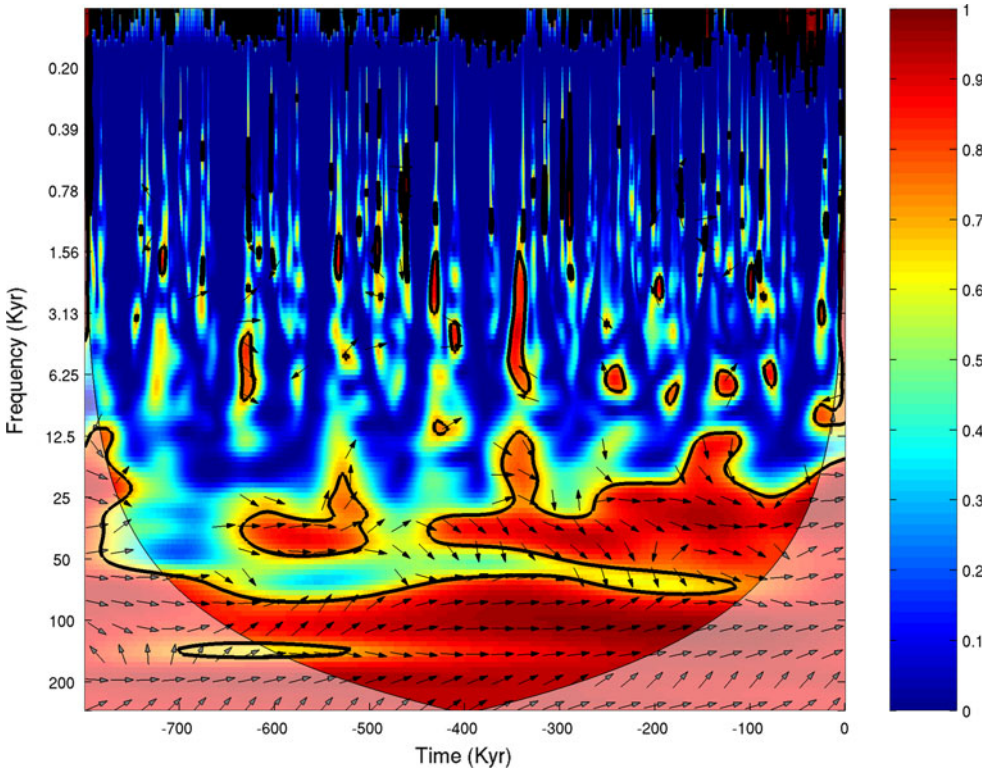

Fig. 17 Wavelet Coherence of CO_2 and C calculated by the 3τ model

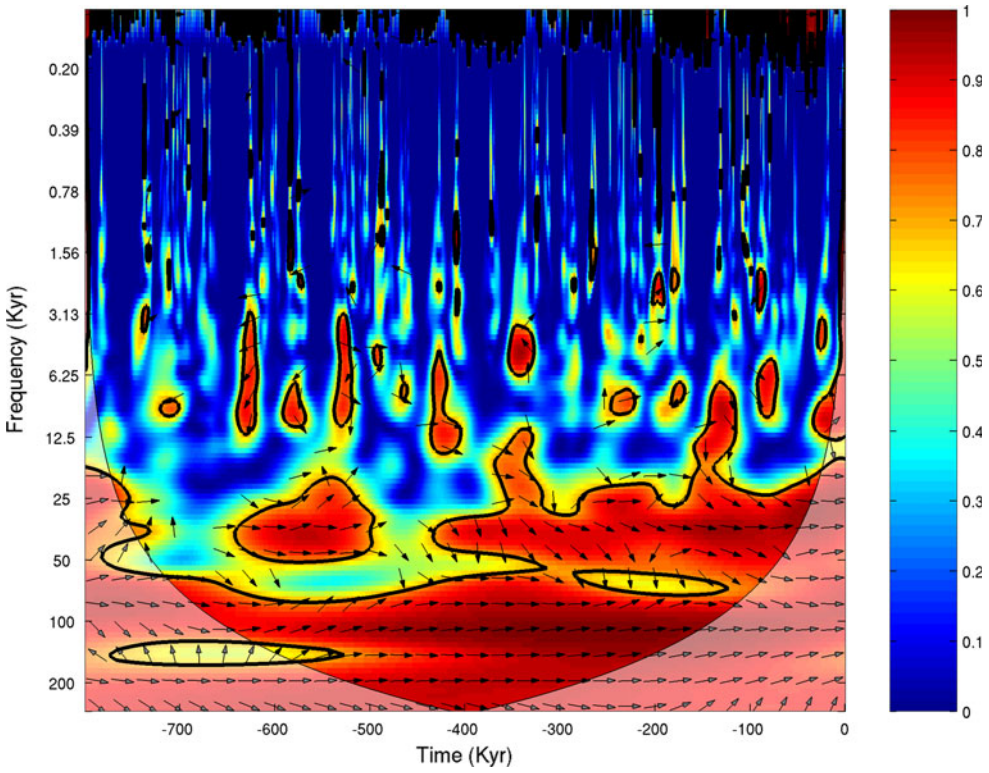

Fig. 18 Wavelet Coherence of CO_2 and C calculated by the LS model

The first step is to see whether the attractor of the observational time series is embedded in a phase space with the same dimensionality as the predicted time series. The dimensionality D obtained for the observational time series, with the method of false nearest neighbors (Marwan 2007), was $D = 4$. The dimensionality D_s obtained for the simulated time series was $D_s = 3$. The difference may be due to the existence of some independent variable not taken

into account by the model that generates the oscillations of a period <2 kyr in $\delta^{18}O$. A moving average of the observational series with a 2-kyr window produced a smoothed time series which generates a dimensionality coincident with the one of the simulated time series ($D = D_s = 3$).

Reconstructed attractors for the smoothed $\delta^{18}O$ and V time series simulated by the 3τ model are displayed in Figs. 19 and 20, respectively. The attractor obtained for LS is almost identical to the one displayed for 3τ. PP04-derived models are forced externally by I_{65} insolation, and a similar astronomical forcing is supposed to act on the climate system. In any externally forced dynamical system one of the dimensions has to be the phase of the external forcing, ϕ, which allows the system to become autonomous through the equation $d\phi/dt = 1$. Two additional variables, v_1 and v_2, remain available, so our three variables V, C and A must be considered as dependent on v_1 and v_2: $V = V(v_1, v_2)$, $C = C(v_1, v_2)$ and $A = A(v_1, v_2)$.

These attractors (Figs. 19 and 20) and the series that they produce bear some resemblance to the Duffing dynamical system, which is a three-dimensional externally forced nonlinear oscillator with an embedded *strange* attractor.

We then obtained the cross recurrence plot (CRP) of observational and simulated trajectories which, despite its name, do not represent recurrences but rather the conjunctures of states of the two systems. The CRP reveals all the times when the phase space trajectory of the first system visits roughly the same area in the phase space where the phase space trajectory of the second system is (Marwan 2007). Figures 21 and 22 show the CRP obtained with the above parameters for the simulated series of V obtained by the 3τ and LS models. The Matlab tool created by Marwan (2007) was used. The data corresponding to the last glacial cycle were not used by the algorithm because the position of the end of the series in relation to these data is smaller than D times l, where D is the dimension (3) and l is the lag (1,433).

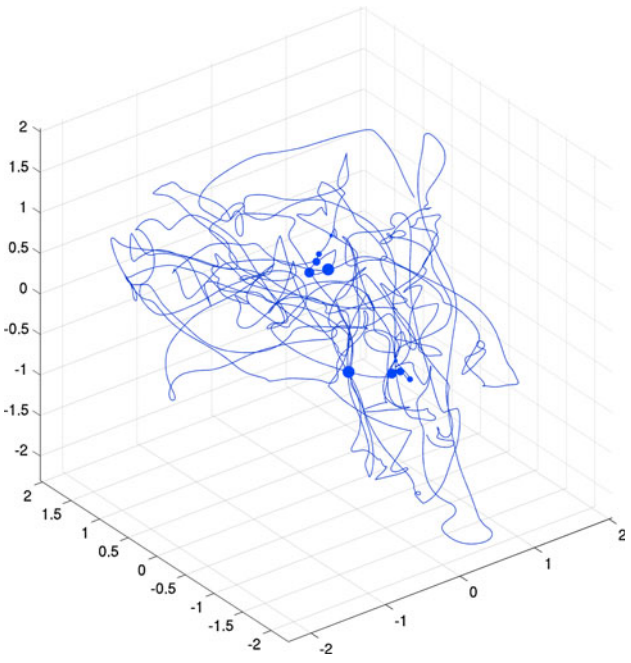

Fig. 19 Embedded attractor of the $\delta^{18}O$ series smoothed with a 2 kyr moving average

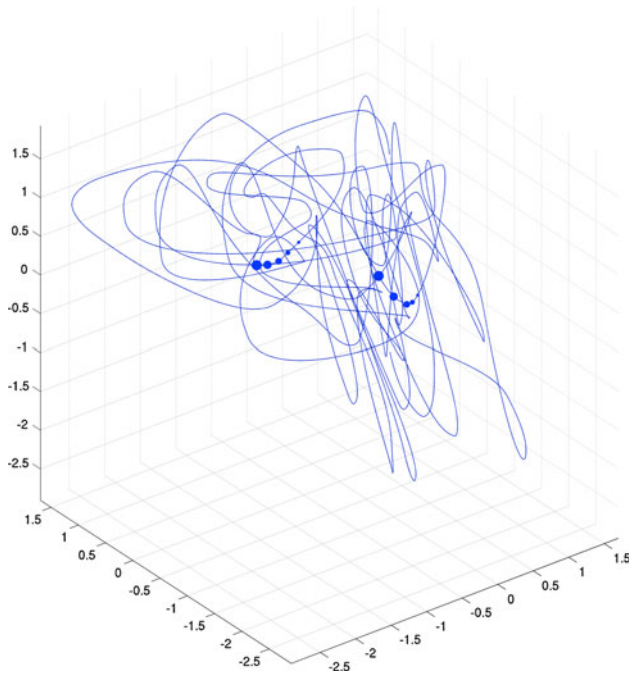

Fig. 20 Embedded attractor of the V variable simulated by the 3τ model

We can see that the persistent intervals of good coincidence between the V and $\delta^{18}O$ series (Fig. 1) coincide with intense black patches in Figs. 21 and 22, especially spots following Termination IX and Termination VII, $5{,}000 < N < 6{,}000$, $7{,}000 < N < 9{,}000$, $9{,}200 < N < 9{,}500$, $1{,}050 < N < 11{,}000$ and $11{,}500 < N < 12{,}500$.

Many patterns occurring in the main diagonal appear deformed in lines and columns, indicating that both series are cyclical and the way in which $V(t)$ coincides with $\delta^{18}O(t)$ at time t shows similarity to the way in which $V(t)$ coincides with $\delta^{18}O(t–T)$, where T is the 100-kyr period.

Roughly 85 % of the time the predicted and observational V trajectories are neighbors at a distance of 0.46 times the standard deviation of the phase space. The C trajectories are much more poorly simulated, with the predicted and observational trajectories being neighbors less than 50 % of the time (Figs. 23 and 24). However, the dynamics in the intervals when the CO_2 is maximum is normally well simulated, which seems to be sufficient to

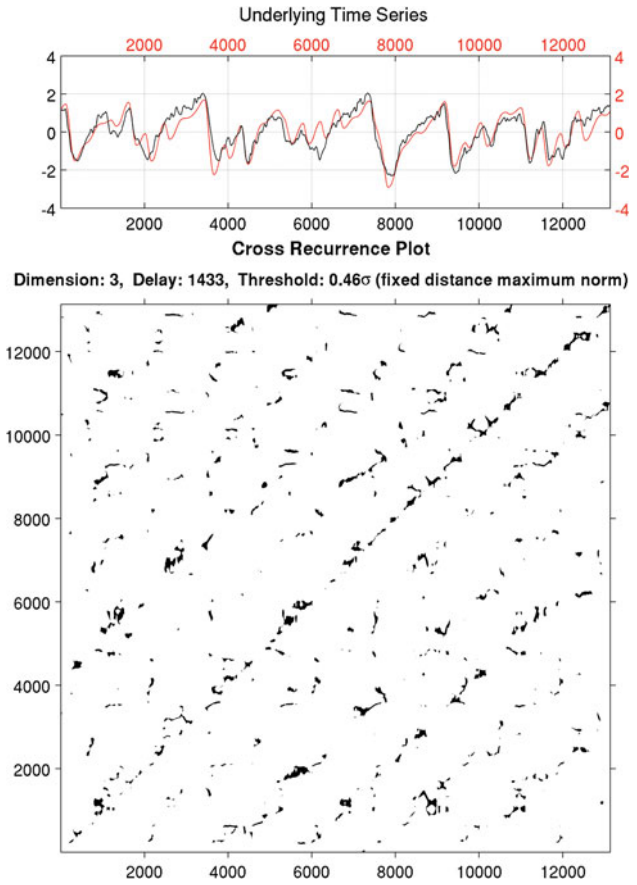

Fig. 21 Cross-recurrence plot of the V variable simulated by the 3τ model

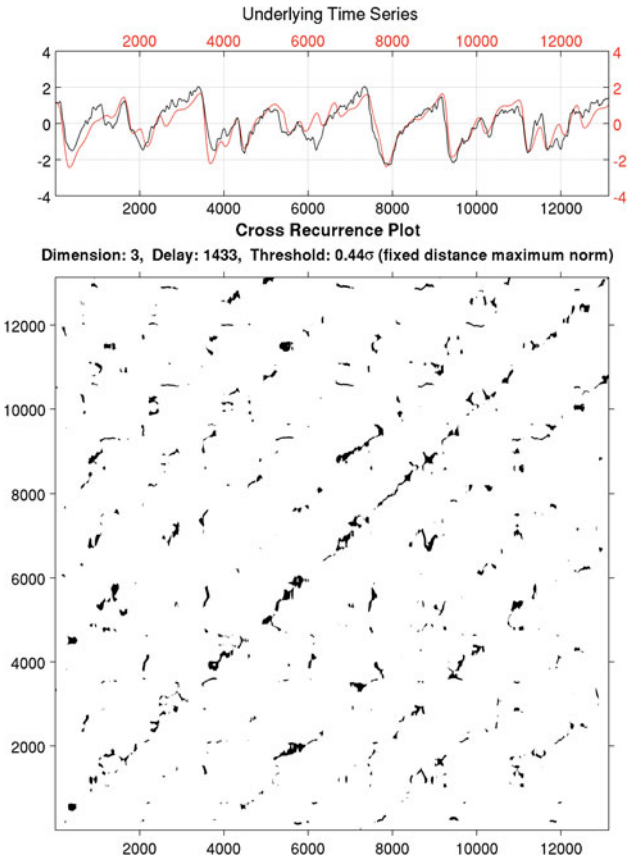

Fig. 22 Cross-recurrence plot of the V variable simulated by the LS model

allow the V dynamics to obtain a good similarity to the observational dynamics.

Online Materials summarizes the information obtained from these tools for model 4τ in its Figs. 5, 6, 7, 8, 9, 10, 11, 12, 13, 14.

A common feature of 3τ and LS models is their lack of sensitivity to the I_{60} forcing. This result could be interpreted in three alternative ways: (i) Our function $F(V, A)$ is an approximate representation of stratification but I_{60} is not a good proxy for Southern Ocean temperature; (ii) stratification and/or CO_2 release in the SO is not controlled by regional temperature; (iii) release of CO_2 in the SO is not controlled by stratification and the function $F(V, A)$ in our models represents a different process.

A possible interpretation belonging to group (iii) is that A might represent sea ice instead of the ice-sheet area and that $F(V, A, I_{60})$ could be a proxy for a rate of emission of CO_2 that is controlled directly by the sea ice area, A, and SO deep temperature. SO deep temperature could be controlled by NH temperature (through V) more strongly than by I_{60}. One possible mechanism able to produce this effect was proposed by Gildor and Tziperman (2001): stratification in the SO is composed of cold, fresh and therefore light water above warm, salty and therefore dense water. Glacial conditions in the northern hemisphere cool the NADW and, consequently, via the southward flow and upwelling of NADW, lower the deep temperature in the SO. Because of the permanent ice cover over Antarctica, surface ocean temperature in the SO near Antarctica is close to freezing point during the entire glacial cycle, so it cannot cool very much even during glacial conditions. Glacial conditions therefore increase the density of deep SO water but not of surface SO water and this strengthens the vertical stratification there. As a result, vertical mixing in the SO is expected to be reduced. This mechanism implies that temperature changes in the Northern Hemisphere (NH) (supposedly correlated with global ice volume V) lead to CO_2 changes in the Southern Hemisphere (SH). This mechanism is plausible but interpreting F as a model for such mechanism is forced, because correlation between V and NA temperature time series (Bard 2003) is low: only 0.64 for last 800 kyr.

On the other hand, to determine whether A is sensitive to I_{60}, Eq. (1b) of the model was modified in the following way:

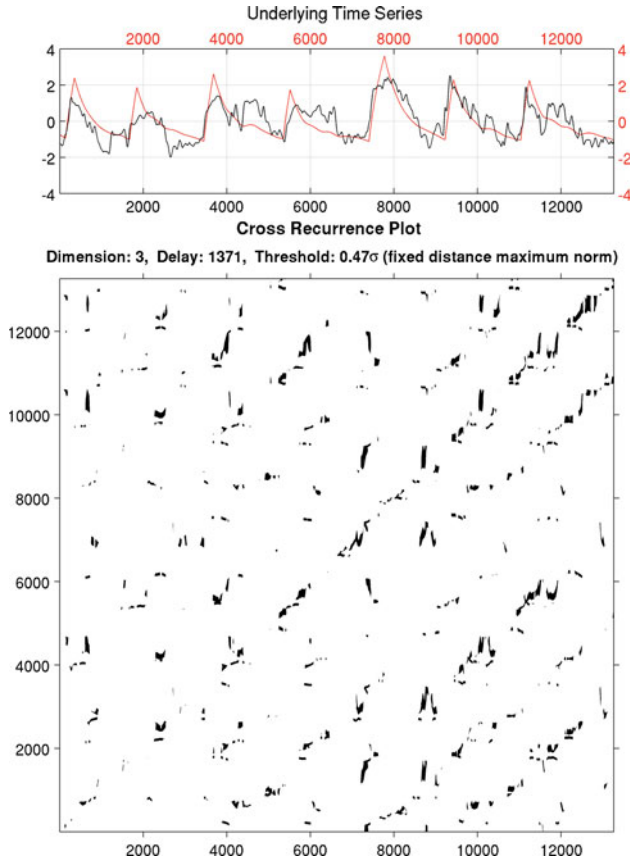

Fig. 23 Cross-recurrence plot of the C variable simulated by the 3τ model

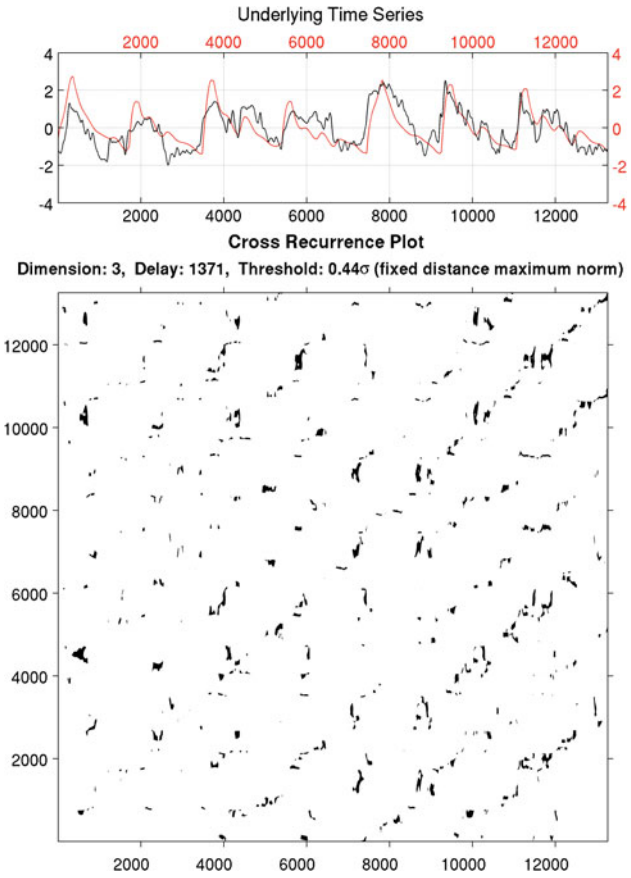

Fig. 24 Cross-recurrence plot of the C variable simulated by the LS model

$$dA/dt = (V - A - cI_{60})/\tau_A$$

However, the best fits obtained after this change did not improve upon those obtained by our 3τ model, showing that Eq. (1b) is also insensitive to I_{60}.

These results are consistent with the following conclusions: A variable A that follows the evolution of V with a delay of 5–7 kyr seems necessary to obtain good fits. This variable can be interpreted, as Paillard and Parrenin (2004) do, as the ice sheet extent on the Antarctic shelf, but it can also be interpreted as the whole SO ice extent since the capping effect mentioned in the Introduction (item (d)) and the control of A on the residual circulation (see Discussion and Conclusions section) act in the same direction as the deep stratification. CO_2 release to the atmosphere in the SO may be controlled by either stratification or sea ice extent, or by both. However, neither of the two corresponding variables in our models (F and A) seems to be sensitive to I_{60} insolation. Either some of these mechanisms are not sensitive to SO temperature, which is difficult to conceive, or I_{60} is not a good proxy for SO temperature.

Huybers and Denton (2008) pointed out an important fact that had gone unperceived and can bring new light to these conclusions: Antarctic summer duration is highly correlated with I_{65} insolation. In addition, it is plausible that the Antarctic climate remains in near radiative equilibrium with local heat accumulation, which is controlled by summertime duration. In contrast, northern changes are mediated through the response of the northern ice sheets, which are much more sensitive to insolation at the solstice (I_{65}) than to summertime duration. Thus, SO temperature could be a crucial variable that has influence on the southern sea ice or the density of deep water, or both; but this southern temperature does not need to be controlled via teleconnection with the north. It may respond to some regional astronomical forcing different to I_{60}.

The correlation between the observational CO_2 time series that we are using and the Antarctic temperature inferred from the EPICA dome by Jouzel et al. (2007) for the past 800 kyr is 0.89. Thus, the good performance of the LS model, where $F = F(C, A)$, and the fact that C is a good proxy of Antarctic temperature, suggest that formation of Antarctic deep waters may be controlled only by ice sheet extent and regional temperature.

The good performance of the 3τ and 4τ models and their functional form $F(V, A)$ could suggest that stratification is partly controlled by the temperature of the NADW

upwelling, through V and the teleconnection mechanism of Gildor and Tziperman (2001). This contribution could exist but it cannot be great because of the modest correlation between the $\delta^{18}O$ and NA sea surface temperature (0.64). More plausibly, $F(V, A)$ is another way to suitably represent stratification in PP04-derived models, since the correlation of $\delta^{18}O$ with Antarctic temperature is almost as high as that of CO_2 (0.86 instead of 0.89). More importantly, the 3τ model simulates V with a far better correlation (0.88) than that of C (0.79) and therefore the correlations between its simulated C and $-V$ and the Antarctic temperature are very similar: 0.78 and 0.77, respectively. Thus, V is a good proxy of SO regional temperature and the expression $F(V, A)$ is plausibly a suitable way to model the local formation of brines, as $F(C, A)$ is. The fact that $F(V, A)$ performs somewhat better than $F(C, A)$ could be attributed to the additional (even small) contribution that V has over stratification (through teleconnection) and C does not.

LS model, which uses the expression $F(C, A)$, needs a direct forcing of I_{65} on C. 3τ, which uses $F(V, A)$, doesn't need it, but it has the direct forcing I_{65} on the V variable. This suggests that PP04-derived models need a quick response of regional SO temperature to I_{65} rising, as quick as $\tau_{v2} \cong 3$ kyr in 3τ and $\tau_c \cong 3$ kyr in LS. The coincidence of these two scales reinforces our interpretation of $-V$ and C in F as proxies of SO regional temperatures.

Figure 25 shows the time variation of I_{65} (panel 1), V (panel 2), A (panel 3), C (panel 4) and F (panel 5) simulated by the LS model for the two last glacial cycles. Due to the effect of τ_C, C responds to the I_{65} variations with a certain delay. For this reason, every maximum (minimum) of I_{65} in the figure is followed by a maximum (minimum) of C 5 kyr later. The variations of C are reflected in the F variable which has its maxima and minima in counterphase with C. On the other hand, A responds to C by following its long-term trend (with a delay of 7 kyr approximately) but damping its high-frequency oscillations. When C is low, as in the glacial maximum, A is large, and F is close to the trigger $F \leq 0$. In this situation, any new maximum in I_{65} causes a decrease in F (through C and A) that triggers the oceanic CO_2 pulse, starting the deglaciation. In the case of 3τ an almost parallel description can be made using variable V instead of C.

The double condition for generating a deglaciation is thus the coincidence of a maximum of I_{65} in a period when V is large. This double condition was observed and incorporated by Paillard in some previous models (Paillard 1998).

Figure 26 shows the relative contributions to CO_2 levels of the mechanisms involved, as functions of time, for the 3τ model (panel 1) and the LS model (panel 2). The dashed line represents the $\delta - \beta V$ term in Eq. (3); the continuous thick line represents the deep ocean contribution

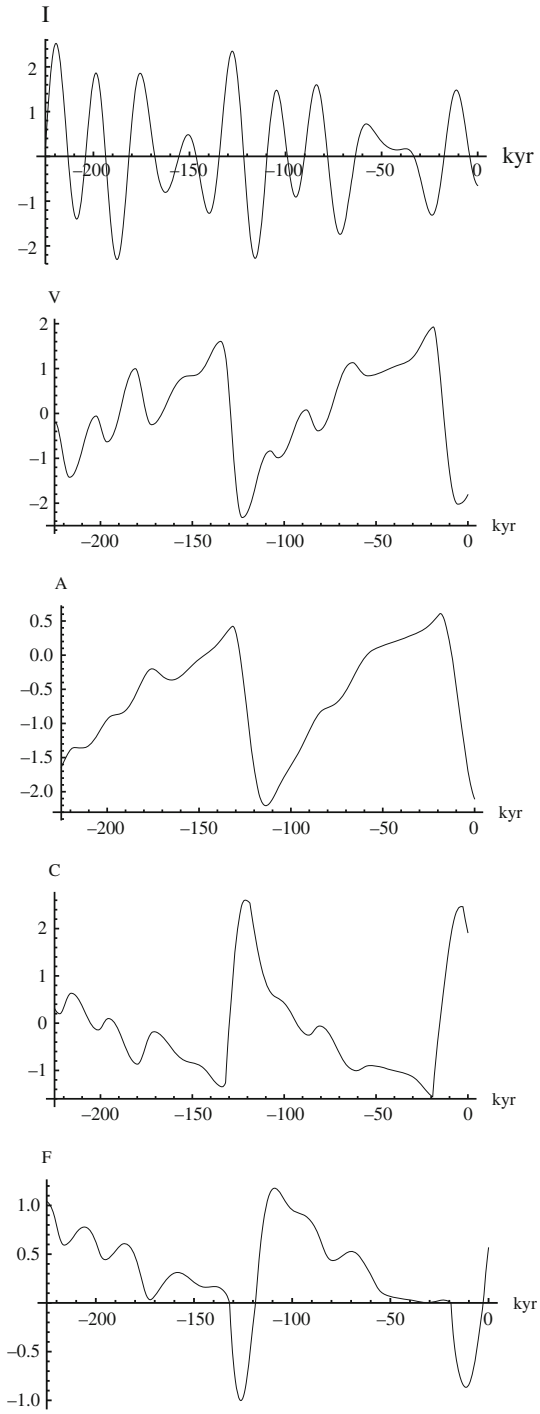

Fig. 25 Time variation of I_{65} (*panel 1*), V (*panel 2*), A (*panel 3*), C (*panel 4*) and F (*panel 5*) simulated by the LS model for the last two glacial cycles

($\gamma P(F) = \gamma H(-F)$ in Eqs. (3) and (8)) to the change in C_r. An inertial contribution, defined as the instantaneous difference between C and its asymptotic value C_r, has been included as a continuous thin line. Units of the horizontal axes are kyr.

The $\gamma P(F)$ contribution has a step-like form even for EP model, where its function $P(F)$ given by Expression (5) and $\lambda = 37$ (Online Materials, Table 1) generates a CO_2 contribution that is very close to simple rectangular functions, as it is in the models displayed in the figure. In conclusion, the oceanic response to deep-water generation efficiency, F, is strongly non-linear in all the models studied, and similar to a single rectangular pulse. In all the models the deglaciations commence following oceanic pulses with duration of 11–20 kyr. In Terminations VIII and VI, the ice volume reduction is smaller than in other terminations, a finding which is produced in our models by a shorter oceanic pulse.

In the 3τ and LS models, C_r maintains a monotonous growth after −135 kyr. First, following the abrupt increase in C_r caused by the connection of the oceanic pulse; then, following the increase in C_r caused by the positive feedback T-CO_2 (V-CO_2 in our models). The slope of this CO_2 increase depends on the rate of decrease of V, which responds to a combination of astronomical forcing and greenhouse feedback. In these models the period during which the CO_2 increases is approximately the period when the oceanic pulse is connected. However, the introduction of a direct forcing of I_{65} on C_r in the LS model allows the deglaciations to start with a shorter oceanic release of CO_2. This interchangeability between a fraction of the oceanic release and other sources of CO_2 taking place at moments of astronomical warming (as the termination periods usually are) stems ultimately from the extreme simplicity of the CO_2 release mechanisms incorporated in the PP04-derived models (see also the Discussion and Conclusions section). After the end of the oceanic pulse and astronomic contributions, C is mainly above its asymptotic level and starts to decrease towards glacial levels.

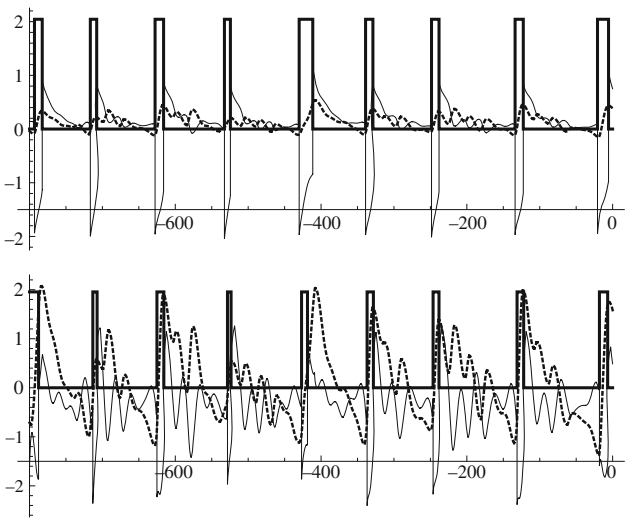

Fig. 26 Relative contributions to CO_2 levels of the mechanisms involved, as functions of time, for the 3τ model (*panel 1*) and the LS model (*panel 2*). The *dashed line* represents the $\delta - \beta V$ term in Eqs. (3) and (8); the continuous *thick line* represents the oceanic contribution to the change in C_r. An inertial contribution, defined as the instantaneous difference between C and its asymptotic value C_r, has been included as a continuous *thin line*. Units of the *horizontal axes* are kyr

Two main conclusions can be extracted from this analysis: (i) The oscillation in V that characterizes the termination periods is essentially produced by the same positive feedbacks, CO_2-T and T-CO_2, that characterize any other oscillation triggered by insolation change; however, this oscillation has stronger slopes in both C_r and V_r because of the extra contribution generated by the oceanic pulse. (ii) A rather abrupt oceanic release of CO_2 (similar to a rectangular pulse) seems necessary to initiate a deglaciation; this release is controlled by the deep-water formation variable, F, which depends mainly on V and A (3τ), or on C and A (LS), and V, A and C are driven in the last term by I_{65} insolation.

5 Observational dynamics

The dynamics and change of overturning, and its impact on CO_2 variation during glacial cycles remain controversial (Sigman et al. 2010). However some facts are well established and widely accepted.

First, the deep ocean has northern and southern meridional overturning circulations (NMOC and SMOC) which have been described as: (i) a long loop dominated by NADW, which is relatively poor in dissolved CO_2 because of high photosynthetic consumption; and (ii) a short loop dominated by AABW which is richer in CO_2 (Toggweiler et al. 2006; Watson and Naveira 2006). The existence of the SMOC loop seems to depend crucially of diapycnal mixing (Haertel and Federov 2012). Both loops mix in the interior around the Antarctic continent to form Circumpolar Deep Water (CDW), which comes up to the surface along the southern part of the Antarctic Circumpolar Current (ACC). This upwelling is forced mainly by the divergence of Ekman pumping at the surface, centered to lie at approximately 65°S today (Toggweiler 1999), which is driven by the mid-latitude westerlies. Any change in either zonal wind stress curl or latitude of the westerly wind belt should reduce the deep water content of the Meridional Overturning Circulation (MOC) and plausibly its intensity (Toggweiler et al. 2006). However, NMOC intensity in the SO seems to be the sum of the mean Ekman transport and opposing mean eddy transport over the ACC. The residual northward transport is strongly controlled by heat gain of the waters travelling northward (Karsten and Marshall 2002).

Second, temperatures are close to freezing at all the sites in the glacial ocean, but the deep SO (at sites located within

present AABW spreading pathways) was much more saline than today, which implies a density anomaly between the deep SO and surface waters that is three times larger than today (Adkins et al. 2002; Watson and Naveira 2006). This evidence could be a consequence of increased brine rejection in Antarctica in combination with reduced recirculation of AABW to the surface (Fischer et al. 2010).

Third, overturning was nearly, or completely, eliminated during the coldest deglacial interval in the North Atlantic region, beginning with the catastrophic iceberg discharge Heinrich event H1, 17,500 years ago (McManus et al. 2004), coinciding with the first major step in Antarctic warming (Barker et al. 2009). Some terminations have started in coincidence with Heinrich events (Cheng 2009). In Terminations I (T–I) and III the same sequence is observed: a Heinrich event at the end of the glacial period (HS1 in T–I), followed by an interstadial (Bolling-Allerod in T–I), lasting 1,800–2,000 years, then a second stadial (Younger Dryas (YDS) in T–I) and then the final deglaciation (Holocene in T–I).

Coupled general circulation models for glacial conditions show very little change in the strength of the zonal wind stress on the SO and weak shifts in the location of the westerlies belt (Fischer et al. 2010). However, observations of wind and rain patterns in HS1 and YDS suggest that the Inter-tropical Convergence Zone (ITCZ) and trade winds shifted southward (Peterson et al. 2000; Leduc et al. 2009; Saikku et al. 2009; Wang et al. 2004; Griffiths et al. 2009). Two warming pulses in the SH coincided with HS1 and YDS, respectively, suggesting a north–south connection mechanism such as the bipolar seesaw suggested by Broecker (1998). The $^{231}Pa/^{230}Th$ ratios from core GGC5 off the Bermuda Rise (McManus et al. 2004) reflect a strong reduction in Atlantic overturning circulation during HS1 and a moderate reduction during YDS. In contrast, biogenic opal flux in the SO, interpreted as a proxy for changes in upwelling south of the Antarctic Polar Front (Anderson et al. 2009) shows an increase in upwelling during HS1, a decrease during the Bolling-Allerod period and a further increase in overturning during YDS. This suggests that the shutdown in the Atlantic Meridional Overturning Circulation (AMOC) removed a source of dense water to the ocean interior and that this "density vacuum" (Broecker 1998) precipitated an increase in AABW formation to fill that vacuum (Sigman et al. 2010).

These pieces of evidence have been interpreted similarly by different authors (see Cheng 2009; Denton et al. 2010; Shakun et al. 2012). The sequence of events would start with a rising boreal summer insolation controlled mainly by inclination and precession cycles (Huybers 2011). This insolation produces a gradual northern warming in the presence of a massive, isostatically depressed NH ice sheet which has growth gradually for 80–100 kyr. In these conditions, an ice instability mechanism makes the Laurentide, Greenland and European sheets ablate and collapse locally, producing a strong meltwater pulse into the North Atlantic, which initiates a Heinrich event. This slows the AMOC and lowers the south-north Atlantic heat flux, with stadial conditions in the north and southern warming and southward movement of climatic zones in the SH. The above three studies agree that this sequence is the deglacial trigger.

A number of mechanisms are potentially able to connect this trigger with an increased release of CO_2 in the SO and subsequent atmospheric CO_2 rise:

(i) Southward movement of climatic zones could include a southward shift in the westerlies, resulting in enhanced wind-driven upwelling on the Antarctic divergence (Marchitto et al. 2007). This would promote ventilation of CDW and the observed productivity peak (Anderson 2009), would erode the Antarctic salinity-driven stratification and would thus facilitate the formation of deep water in Antarctica (Toggweiler et al. 2006). However, the importance of this mechanism is not clear because there is no evidence of substantial variation in the strength of the AMOC during the glacial, which was probably only slightly weakened in comparison with today (Lynch-Stieglitz et al. 2007) though it formed a shallower Glacial North Atlantic Intermediate Water (GNAIW) (Sigman et al. 2010).

(ii) Warming of the SO could melt sea ice, leading to an increase in ventilation as a result of enhanced residual northward transport and also to degassing effects. As suggested by Fischer (2010), the increase and decrease in sea ice coverage could have modulated the annual net heat gain of the SO surface, and the reduced buoyancy gain would have weakened the MOC during glacial periods through its control of the residual circulation. This would have limited the upwelling of CO_2-enriched deep water, acting in the same direction as the capping effect that winter ice extent is assumed to have on deep-water outgassing of CO_2 (Stephens and Keeling 2000).

(iii) Warming associated with southerly shifts could reduce Patagonian glaciation, lowering the flux of dust and iron from Patagonia to the SO. This would reduce the efficiency of the biological pump (Martin and Fitzwater 1988).

(iv) Increased CO_2 release from Antarctic divergence would decrease the concentration of dissolved inorganic carbon (DIC) and thus increase the carbonate ion concentration in the deep ocean. This would increase the burial rate of calcium carbonate, forcing a decrease in whole-ocean alkalinity, decreasing

solubility and putting an additional fraction of CO_2 into the atmosphere. According to Sigman et al. (2010), this carbonate compensation in cooperation with switch on/off of deep water formation or a degassing effect is able to account for 40 ppm of pCO_2 difference between interglacial and glacial conditions. It is probable that neither Antarctic overturning nor gas exchange were completely shut off/on. However, more complete nutrient consumption and lower export of organic matter have been observed in the Antarctic during glacial periods, suggesting a reduced supply of nutrients and water from the deep to the surface ocean (Sigman et al. 2010). Thus, overturning decreased in the glacial SO while productivity did not decrease as much as the nutrient supply from below did, making pCO_2 decrease as a result. This mechanism would have complemented the previous ones, generating the atmospheric pCO_2 difference of 40 ppm.

(v) In the sub-Antarctic zone, the sinking flux of organic matter was greater in glacial periods than today, with some evidence for more complete nutrient consumption (Sigman et al. 2010). The effect of this zone on alkalinity and availability of nutrients at low-latitudes is great, reaching 40 ppm for the pCO_2 glacial-interglacial difference (Hain et al. 2010).

As observed by Sigman et al. (2010) the declines in atmospheric pCO_2 to their minima during peak ice ages tend to occur over tens of thousands of years and/or in steps. This may result from the progressive activation of different pCO_2 reducing processes (Hain et al. 2010). In particular, the Antarctic cooling early in the last ice age, 115 kyr BP, has been interpreted as reduced Antarctic overturning or increased sea-ice suppression of gas exchange (Peacock et al. 2006) with an additional fraction of CO_2 uptake due to ocean cooling. In contrast, the second major decline in atmospheric pCO_2, 70 kyr BP, coincides with a major dust flux increase in Antarctic and sub-Antarctic zones (Martínez García 2009), which may have caused iron fertilization of the SO (Watson et al. 2000). Additionally, this period may have suffered the sharpest transition from NADW to GNAIW formation (Hoddell et al. 2003), which may have improved the ability of the deep SO to lower atmospheric pCO_2 (Sigman et al. 2010).

6 Discussion and conclusions

To what extent are PP04-derived models consistent with the observational dynamics summarized in Sect. 5? First, the sequence of activation of processes that release CO_2 during the terminations, suggested by the triggering sequence mentioned above, is very different to the sequence of steps that reduce CO_2 during glacial times, which we discussed at the end of Sect. 5, and this difference generates the typical saw-tooth shape of the CO_2 glacial-interglacial oscillations. The lack of a complete model for the biological and carbonate pumps in the PP04-derived models makes it impossible to precisely reproduce the series of events that characterize glacial periods, and using different relaxation times for moments of increasing and decreasing CO_2 is the easiest way to take into account this asymmetry and to reproduce the double slope cycle. When a single relaxation time τ_C is used ($\tau_{C2} = 0$) in the LS calibration, the correlation obtained for V decreases by less than 1 % (0.85 instead of 0.86) but the correlation for C decreases by 8 % (0.68 instead of 0.74) because of the far more abrupt ups and downs of the simulated C during the glacial periods. The 3τ model is much less sensitive to this τ_{C2} parameter, and maintains a very high correlation when it is eliminated (0.88 and 0.79, for V and C, respectively, in the 3τ model). We thus obtained a model with almost the same correlations as 4τ and with one parameter less than PP04. The good performance in relation to PP04 must be attributed only to the introduction of a different time for accumulation (τ_V) and for ablation of ice (τ_{V2}).

Though the glacial decay is only roughly simulated by PP04-derived models, the precise fitting of pace and intensity of interglacial CO_2 that these models generate are sufficient to allow the models to obtain a good match of the ice volume evolution.

The term cI_{60} has been maintained in Eq. (4) to clarify the discussion, but one conclusion of this study is that PP04-derived models are not sensitive to I_{60} southern insolation. In these models, C seems to be a much better proxy of Antarctic temperature than I_{60} is. This indirectly reinforces the claim of Huybers and Denton (2008) that Antarctic temperature is not sensitive to insolation during a particular summer day and that it could be sensitive to another kind of variable, such as austral summer duration.

The stratification function, F, is a crucial variable of PP04-derived models, which must be interpreted as stratification produced by density difference between AABW and NADW with a possible minor contribution from stratification produced by density difference between NADW and surface water. F controls the upwelling of CO_2 in a nonlinear way: an abrupt oceanic release of CO_2 similar to a rectangular pulse of 10–20 kyr and very sensitive to F is necessary in these models to generate the terminations. There are reasons to believe that mixing rates may decrease as density differences increase (Watson and Naveira 2006) if we use the internal wave parameterization for the vertical mixing coefficient suggested by Gargett (1984). If the density difference between AABW and

NADW is small, the blending process of the two water masses may be more efficient and a larger fraction of the AABW wells up with the mixed Lower Circumpolar Deep Water (LCDW) into the two loops of the meridional overturning circulation (NMOC and SMOC). Bouttes et al. (2012) have shown the plausibility of this stratification-dependent mechanism with a model of intermediate complexity.

PP04-derived models need a quick response of regional SO temperature (represented by C in LS and by $-V$ in 3τ) to I_{65} rising, as quick as $\tau_{v2} \cong 3$ kyr in 3τ and $\tau_c \cong 3$ kyr in LS. The real climate system could produce a quick response of this kind during deglaciations by the bipolar seesaw mechanism (Broecker 1998).

A is another crucial variable for this kind of models and follows the evolution of V and C with a delay of about 5–7 kyr. This dependence shows that A is sensitive to Antarctic temperature, and its delay suggests that A represents extent of ice sheet on Antarctic shelves and not SO sea ice extent. Polynyas are the places where most of the brine is produced and are located between the ice sheet edges and sea ice. Thus, the position of ice-sheet boundaries is crucial for the rate and density of the deep water formed. According to Anderson et al. (2002), the Antarctic ice-sheet edge was close to the continental slope in the LGM and it started to retreat onto the continent some thousand years after the LGM on most of the shoreline. This delay seems to be coherent with the delay obtained for the A variable in our calibrations. Therefore, PP04-derived models reinforce an interpretation of the oceanic CO_2 release during deglaciations as controlled by deep stratification rather than by a capping effect.

As can be observed in Fig. 25 (panel 3 and 5), A takes about 80–100 kyr to reach a level that makes stratification become critical ($F < 0$). Therefore, the 100-kyr period that is the main frequency of glacial cycles must be considered as internally generated by the climate system. More specifically, it must be interpreted as the characteristic time needed for the Antarctic ice sheet to reach the continental slope. The observations of Anderson et al. (2002) on the advance and retreat of ice shelves are not in disagreement with this time scale, but additional observations are needed to contrast this prediction of PP04-derived models.

According to Tziperman et al. (2006), many of the models that best fit glacial oscillations have a "phase locking" between a Milankovitch frequency ω_m and an internal cyclicity ω_i. Frequently, a good fit can be obtained when the quotient ω_m/ω_i is a rational number. However, this "good" fit does not imply that the mechanisms represented by the model are the correct ones. Phase locking is a necessary condition but not a sufficient one. However, Tziperman et al. (2006) conclude that "the actual glacial cycles may also be similarly phase locked to the Milankovitch forcing". That is, this property is probably also one of the climate system itself. If this is so, showing nonlinear phase locking is a good—though not sufficient—feature for a correct paleoclimate model.

What should be sufficient? There is no clear mathematical criterion for deciding. However, if the right mechanisms were to be incorporated in a model with nonlinear locking, we would expect from it the following features: (i) its predictions should have higher correlations with the experimental time series; (ii) it should reproduce the ups and downs of the experimental time series in the scales between 10^3 and 10^6 years better than other models of similar complexity; and (iii) it should generate time series with frequency composition and embedding dynamics similar to the observational ones. However, ultimately, only the experimental confirmation that the proposed mechanisms are really acting would be a definitive sufficient condition.

The visual inspection of Figs. 1 and 2 as well as the good correlations obtained show that they offer great improvements in criteria (i) and (ii) in comparison with other simple models studied in the literature. The wavelet analysis and phase space portraits show that the models that we have discussed here satisfy the third criteria, at least for variable V. On other hand, the pace of orbital timescale is well simulated for V and C, but in the sub-orbital timescales the phasing of C is poorly matched in many periods that include the deglaciations (Figs. 17 and 18). In addition, the cross-recurrence analysis shows that the short term coherence between simulated and observational CO_2 is only sporadic, indicating that both time series do not follow the same dynamical behavior (Figs. 23 and 24). However, in the deglacial periods the two carbon series become dynamically close. Finally, neither simulated C nor V match the observations on timescales 1–10 kyr, which are the timescales where the first events of the deglacial trigger take place.

The most important conclusion of this study is that a detailed dynamics of CO_2 is of little relevance to obtain very good agreement between simulated ice volume and $\delta^{18}O$. All that is needed is a nonlinear instability that is reached after 80–100 kyr and that enables that even a modest sub-orbital variation may trigger a sudden release of atmospheric CO_2. This nonlinear instability seems to be controlled by V or C (here interpreted as Antarctic temperature) and by A (interpreted as Antarctic ice sheet) in PP04-derived models. More specifically, Antarctic cooling would press toward greater stratification because a cooler regional temperature would precondition the surface layer temperature making easier to the water column on the shelf to get the -1.9 to -2°C needed for freezing and brine formation. On the other hand, ice sheet extent would tend to block the active polinyas, producing an opposite effect.

With the progress of glaciation the latter effect would become dominant and would put the system close to the instability, due to the decrease of stratification.

A precise simulation of the detailed set of events constituting the deglacial trigger would require adding some model for the NA ice sheet instability to our models as well as more complex carbon models. PP04-derived models produce good fits in spite of their simplicity in the modeling of oceanic CO_2 release, which is made to depend only on stratification. The other contributions (carbonate compensation, shoaling or deepening of NA deep-water formation, change of productivity in SO and slowing down of SO overturning) are not included in the model, but should be included in future improvements to obtain a closer representation of all the physical processes that are apparently involved.

More specifically, Heinrich events seem to belong to a cyclic process of calving with a recurrence period much shorter than deglaciations (Bond and Lotti 1995). However, according to the interpretations of Cheng (2009), Denton et al. (2010) and Shakun et al. (2012), Heinrich events are able to produce large iceberg discharges and long stadials only when ice sheets become large enough. Long stadials are needed to produce a strong CO_2 oceanic release able to start the termination according to Denton et al. (2010). However, large oceanic CO_2 emissions can be produced only if stratification has weakened at the end of the glacial period because of the lack of brine formation (Paillard and Parrenin 2004; Bouttes et al. 2012) or may be weakened by the expected SO upwelling activation. Ultimately, stratification change plausibly controls a large fraction of the oceanic CO_2 release and is synchronous with other mechanisms which contribute an additional fraction in warm periods, such as biological and carbonate pumps in the sub-Antarctic zone (Hain et al. 2010; Sigman et al. 2010). In this regard, stratification may play the same role as an "order parameter" (Haken 1987) plays in a synergetic nonlinear change.

Acknowledgments This is a contribution to the TIC-MOC project funded by the 2008–2011 Spanish R + D Plan. We thank Dr. Carles Pelejero and Dr. Eva Calvo for their interesting suggestions and help with the experimental data and to an anonymous reviewer whose exhaustive review contributed greatly to improve the manuscript. The work of one of the authors (C. Herrero) was supported by a CSIC JAE-Predoc scholarship co-financed by the European Social Fund (FSE).

References

Adkins JF, McIntyre K, Schrag DP (2002) The salinity, temperature, and delta O-18 of the glacial deep ocean. Science 298:1769–1773

Anderson JB, Shipp SS, Lowe AL, Wellner JS, Mosola AB (2002) The Antarctic ice sheet during the last glacial maximum and its subsequent retreat history: a review. Quat Sci Rev 21:49–70

Anderson RF, Ali S, Bradtmiller LI, Nielsen SHH, Fleisher MQ, Anderson BE, Burcklel LH (2009) Wind-driven upwelling in the Southern Ocean and the deglacial rise in atmospheric CO_2. Science 323:1443–1448. doi:10.1126/science.1167441

Archer D, Maier-Reimer E (1994) Effect of deep-sea sedimentary calcite preservation on atmospheric CO_2 concentration. Nature 367:260–263

Bard E (2003) North-Atlantic Sea surface temperature reconstruction, IGBP PAGES/world data center for paleoclimatology. Data Contribution Series #2003-026. NOAA/NGDC Paleoclimatology Program, Boulder CO, USA

Bard E, Hamelin B, Arnold M, Montaggioni L, Cabioch G, Faure G, Rougerie F (1996) Deglacial sea-level record from Tahiti corals and the timing of global meltwater discharge. Nature 382:241–244

Barker S, Diz P, Vautravers MJ, Pike J, Knorr G, Hall IR, Broecker WS (2009) Interhemispheric Atlantic seesaw response during the last deglaciation. Nature 457:1050–1097

Berger A (1978) A simple algorithm to compute long term variations of daily or monthly insolation. Contr. 18. Inst of Astronomy and Geophysics. Universite Catholique de Louvain. Louvain-la-Neuve. Belgium

Berger A, Loutre MF (1991) Insolation values for the climate of the last 10 million years. Quat Sci Rev 10:297–317

Bintanja R, van de Wal RSW, Oerlemans J (2005) Modelled atmospheric temperatures and global sea levels over the past million years. Nature 437:125–128. doi:10.1038/nature03975

Bond GC, Lotti R (1995) Iceberg discharges into the North Atlantic on millennial time scales during the last glaciation. Science 267:1005–1010. doi:10.1126/science.267.5200.1005

Bouttes N, Paillard D, Roche DM, Waelbroeck C, Kageyama M, Lourantou A, Michel E, Bopp L (2012) Impact of oceanic processes on the carbon cycle during the last termination. Clim Past 8:149–170

Broecker WS (1971) A kinetic model for the chemical composition of sea water. Quat Res 1:188–207

Broecker WS (1982) Glacial to interglacial changes in ocean chemistry. Prog Oceanogr 11:151–197

Broecker WS (1998) Paleocean circulation during the last deglaciation: a bipolar seesaw? Paleoceanography 13:119–121

Cheng H (2009) Ice age terminations. Science 326:248–252. doi:10.1126/science.1177840

Denton GH, Anderson RF, Toggweiler JR, Edwards RL, Schaefer JM, Putnam AE (2010) The last glacial termination. Science 328:1652–1656

Fischer H, Schmitt J, Luthi D, Stocker TF, Tschumi T, Parekh P, Joos F, Kohler P, Volker C, Gersonde R, Barbante C, Le Floch M, Raynaud D, Wolff E (2010) The role of Southern Ocean processes in orbital and millennial CO_2 variations: a synthesis. Quat Sci Rev 29:193–205

François R, Altabet MA, Yu EF, Sigman DM, Bacon MP, Frank M, Bohrmann G, Bareille G, Labeyrie LD (1997) Contribution of Southern Ocean surface-water stratification to low atmospheric CO_2 concentrations during the last glacial period. Nature 389:929–935. doi:10.1038/40073

García-Olivares A, Herrero C (2012) Fitting the last Pleistocene $\delta^{18}O$ and CO_2 time series with simple box models. Scientia Marina 76S1:209–218. doi:10.3989/scimar.03617.19H

Gargett AE (1984) Vertical eddy diffusivity in the ocean interior. J Mar Res 42:359–393

Gildor H, Tziperman E (2001) Physical mechanisms behind biogeochemical glacial-interglacial CO_2 variations. Geophys Res Lett 28:2421–2424

Griffiths ML, Drysdale RN, Gagan MK, Zhao J-X, Ayliffe LK, Hellstrom JC, Hantoro WS, Frisia S, Feng Y-X, Cartwright I, St. Pierre E, Fischer MJ, Suwargadi BW (2009) Increasing

Australian-Indonesian monsoon rainfall linked to early Holocene sea-level rise. Nat Geosci 2:636–639. doi:10.1038/NGEO605
Grinsted A, Moore JC, Jevrejeva S (2004) Application of the cross wavelet transform and wavelet coherence to geophysical time series. Nonlinear Process Geophys 11:561–566
Haertel P, Federov A (2012) The ventilated ocean. J Phys Oceanogr 42:141–164
Hain MP, Sigman DM, Haug GH (2010) Carbon dioxide effects of Antarctic stratification, North Atlantic Intermediate Water formation, and subantarctic nutrient drawdown during the last ice age: diagnosis and synthesis in a geochemical box model. Global Biogeochem Cycles 24. doi:10.1029/2010GB003790
Haken H (1987) Advanced synergetics: instability hierarchies of self-organizing systems and devices. Springer, Berlin
Hoddell DA, Venz KA, Charles CD, Ninnemann US (2003) Pleistocene vertical carbon isotope and carbonate gradients in the South Atlantic sector of the Southern Ocean. Geochem Geophys Geosyst 4:1004. doi:10.1029/2002gc000367
Huybers P (2011) Combined obliquity and precession pacing of late Pleistocene deglaciations. Nature 480:229–232. doi:10.1038/nature10626
Huybers P, Denton G (2008) Antarctic temperature at orbital timescales controlled by local summer duration. Nat Geosci. doi:10.1038/ngeo311
Indermühle A, Monnin E, Stauffer B, Stocker TF, Wahlen M (2000) Atmospheric CO_2 concentration from 60 to 20 kyr BP from the Taylor Dome ice core, Antarctica. Geophys Res Lett 27:735–738. doi:10.1029/1999GL010960
Jouzel J, Masson-Delmotte V, Cattani O, Dreyfus G, Falourd S, Hoffmann G, Minster B, Nouet J, Barnola JM, Chappellaz J, Fischer H, Gallet JC, Johnsen S, Leuenberger M, Loulergue L, Luethi D, Oerter H, Parrenin F, Raisbeck G, Raynaud D, Schilt A, Schwander J, Selmo E, Souchez R, Spahni R, Stauffer B, Steffensen JP, Stenni B, Stocker TF, Tison JL, Werner M, Wolff EW (2007) Orbital and millennial Antarctic climate variability over the past 800,000 years. Science 317:793–797
Karsten RH, Marshall J (2002) Constructing the residual circulation of the ACC from observations. J Phys Oceanog 32:3315–33227
Keeling RF, Stephens BB (2001) Antarctic sea ice and the control of Pleistocene climate instability. Paleoceanography 16:112–131
Leduc G, Vidal L, Tacikawa K, Bard E (2009) ITCZ rather than ENSO signature for abrupt climate changes across the tropical Pacific? Quat Res 72:123–131
Lisiecki LE, Raymo ME (2005) A Pliocene-Pleistocene stack of 57 globally distributed benthic delta-18 O records. Paleoceanography 20:PA1003. doi:10.1029/2004PA001071
Lüthi D, Le Floch M, Bereiter B, Blunier T, Barnola J-M, Siegenthaler U, Raynaud D, Jouzel J, Fischer H, Kawamura K, Stocker TF (2008) High-resolution carbon dioxide concentration record 650000–800000 years before present. Nature 453:379–382
Lynch-Stieglitz J, Adkins JF, Curry WB, Dokken T, Hall IR, Herguera JC, Hirschi JJ-M, Ivanova EV, Kissel C, Marchal O, Marchitto TM, McCavel IN, McManus JF, Mulitza S, Ninnemann U, Peeters F, Yu E-F, Zahn R (2007) Atlantic meridional overturning circulation during the last glacial maximum. Science 316:66–69. doi:10.1126/science.1137127
Marchitto TM, Lehman SJ, Ortiz JD, Fluckiger J, van Geen A (2007) A marine radiocarbon evidence for the mechanism of deglacial atmospheric CO_2 rise. Science 316:1456–1459
Martin JH, Fitzwater SE (1988) Iron deficiency limits phytoplankton growth in the North-East Pacific subarctic. Nature 331:341–343
Martínez García A (2009) Links between iron supply, marine productivity, sea surface temperature, and CO2 over the last 1.1 Ma. Paleoceanography 24:14. doi:10.1029/2008pa001657
Marwan N, Romano MC, Thiel M, Kurths J (2007) Recurrence plots for the analysis of complex systems. Phys Rep 438(5–6): 237–329
McManus JF, François R, Gherardi JM, Keigwin LD, Brown-Leger S (2004) Collapse and rapid resumption of Atlantic meridional circulation linked to deglacial climate changes. Nature 428:834–837
Monnin E, Indermühle A, Dällenbach A, Flückiger J, Stauffer B, Stocker T, Raynaud D, Barnola J-M (2001) Atmospheric CO_2 concentrations over the last glacial termination. Science 291:112–114
Paillard D (1998) The timing of Pleistocene glaciations from a simple multiple-state climate model. Nature 391:378–381
Paillard D (2010) Climate and the orbital parameters of the Earth. C R Geosci 342:273–285
Paillard D, Parrenin F (2004) The Antarctic ice sheet and the triggering of deglaciations. Earth Planet Sci Lett 227:263–271
Peacock S, Lane E, Restrepo JM (2006) A possible sequence of events for the generalized glacial-interglacial cycle. Global Biogeochem. Cycles 20:GB2010. doi:10.1029/2005GB002448
Pepin L, Raynaud D, Barnola JM, Loutre MF (2001) Hemispheric roles of climate forcings during glacial–interglacial transitions as deduced from the Vostok record and LLN-2D model experiments. J Geophys Res 106:31885–31892
Peterson LC, Haug GH, Hughen KA, Röhl U (2000) Rapid changes in the hydrologic cycle of the tropical Atlantic during the last glacial. Science 290:1947–1951
Petit JR, Jouzel J, Raynaud D, Barkov NI, Barnola J-M, Basile I, Bender M, Chappellaz J, Davis M, Delaygue G, Delmotte M, Kotlyakov VM, Legrand M, Lipenkov VY, Lorius C, Pépin L, Ritz C, Saltzman E, Stievenard M (1999) Climate and atmospheric history of the past 420,000 years from the Vostok ice core, Antarctica. Nature 399:429–436
Robinson RS, Sigman DM (2008) Nitrogen isotopic evidence for a poleward decrease in surface nitrate within the ice age Antarctic. Quat Sci Rev 27:1076–1090
Saikku R, Stott L, Thunell R (2009) A bi-polar signal recorded in the western tropical Pacific: Northern and Southern Hemisphere climate records from the Pacific warm pool during the last Ice Age. Quat Sci Rev 28:2374. doi:10.1016/j.quascirev.2009.05.007
Sarmiento JL, Toggweiler JR (1984) A new model for the role of the oceans in determining atmospheric P_{CO2}. Nature 308:621–624
Shakun JD, Clark PU, He F, Marcott SA, Mix AC, Liu Z, Otto-Bliesner B, Schmittner A, Bard E (2012) Global warming preceded by increasing carbon dioxide concentrations during the last deglaciation. Nature 484:49–54. doi:10.1038/nature10915
Siegenthaler U, Wenk Th (1984) Rapid atmospheric CO_2 variations and ocean circulation. Nature 308:624–626
Siegenthaler U, Stocker T, Monnin E, Lüthi D, Schwander J, Stauffer B, Raynaud D, Barnola J-M, Fischer H, Masson-Delmotte V, Jouzel J (2005) Stable carbon cycle–climate relationship during the late pleistocene. Science 310:1313–1317
Sigman DM, McCorkle DC, Martin WR (1998) The calcite lysocline as a constraint on glacial/interglacial low-latitude production changes. Global Biogeochem Cycles 12:409–427. doi:10.1029/98GB01184
Sigman DM, Hain MP, Haug GH (2010) The polar ocean and glacial cycles in atmospheric CO2 concentration. Nature 466:47–55
Sowers T, Bender M (1995) Climate records covering the last deglaciation. Science 14:210–214
Stephens BB, Keeling RF (2000) The influence of Antarctic sea ice on glacial-interglacial CO2 variations. Nature 404:171–174
Toggweiler JR (1999) Variation of atmospheric CO_2 by ventilation of the ocean's deepest water. Paleoceanography 14:571–588
Toggweiler JR, Sarmiento JL (1985) Glacial to interglacial changes in atmospheric carbon dioxide: The critical role of ocean surface

water in high latitudes. In: Sundquist E, Broecker WS (eds) The carbon cycle and atmospheric CO2: natural variations archean to present, Geophysical monograph 32. American Geophysical Union, Washington, pp 163–184

Toggweiler JR, Russell JL, Carson SR (2006) Mid-latitude westerlies, atmospheric CO_2 and climate change during the ice ages. Paleoceanography 21, PA2005. doi:10.1029/2005PA001154

Tziperman E, Raymo ME, Huybers P, Wunsch C (2006) Consequences of pacing the Pleistocene 100 kyr ice ages by nonlinear phase locking to Milankovitch forcing. Paleoceanography 21:PA4206. doi:10.1029/2005PA001241

Waelbroeck C, Labeyrie LME, Duplessy JC, McManus JF, Lambeck K, Balbon E, Labracherie M (2002) Sea-level and deep water temperature changes derived from benthic foraminifera isotopic records. Quat Sci Rev 21:295–305

Wang XF, Auler AS, Edwards RL, Cheng H, Cristalli PS, Smart PL, Richards DA, Shen C–C (2004) Wet periods in northeastern Brazil over the past 210 kyr linked to distant climate anomalies. Nature 432:740–743

Watson AJ, Naveira Garabato AC (2006) The role of Southern Ocean mixing and upwelling in glacial-interglacial atmospheric CO_2 change. Tellus 58B:73–87

Watson AJ, Bakker DCE, Ridgewell AJ, Boyd PW, Law CS (2000) Effect of iron supply on Southern Ocean CO2 uptake and implications for atmospheric CO2. Nature 407:730–733